

STARFISH: A COMPACT, BIOMIMETIC, AND ADAPTIVE
SHAPE MEMORY ALLOY ORBITAL DEBRIS REMOVER

By

Katelyn Branaman

A Thesis Submitted to the Faculty of Embry-Riddle Aeronautical University

In Partial Fulfillment of the Requirements for the Degree of

Master of Science in Aerospace Engineering

May 2024

Embry-Riddle Aeronautical University

Daytona Beach, Florida

STARFISH: A COMPACT, BIOMIMETIC, AND ADAPTIVE
SHAPE MEMORY ALLOY ORBITAL DEBRIS REMOVER

By

Katelyn Branaman

This Thesis was prepared under the direction of the candidate's Thesis Committee Chair, Dr. Daewon Kim, Department of Aerospace Engineering, and has been approved by the members of the Thesis Committee. It was submitted to the Office of the Senior Vice President for Academic Affairs and Provost, and was accepted in the partial fulfillment of the requirements for the Degree of Master of Science in Aerospace Engineering.

THESIS COMMITTEE

Chair, Dr. Daewon Kim

Member, Dr. Troy Henderson

Member, Dr. Riccardo Bevilacqua

Graduate Program Coordinator,
Dr. Hever Moncayo

Date

Dean of the College of Engineering,
Dr. James W. Gregory

Date

Associate Provost of Academic Support,
Dr. Kelly Austin

Date

Dedication

To a better tomorrow, as that is the true spirit of engineering.

ACKNOWLEDGEMENTS

Thank you to Dr. Daewon Kim who provided critical guidance for this thesis and countless other projects. Thank you to my committee members Dr. Riccardo Bevilacqua and Dr. Troy Henderson. Thank you to NASA and Orbotics LLC. for their generous support via the SBIR grant. Thank you to my fellow lab workers Nick, Rishi, and Taylor for their wise advice and recommendations. Thank you to my friends and family for their love and continuing support.

ABSTRACT

This thesis aims to turn the tides on the orbital debris issue through the fabrication and demonstration of a compact, biomimetic, and adaptive shape memory alloy actuated orbital debris remover. The design, referred to as Starfish, is discussed in detail along with its fabrication process and object capture ability. A hard skeleton crafted from PETG was combined with shape memory alloy wires and extension springs to create a biomimetic structure that operates similar to the human hand, capable of gripping a wide range of objects. Relevant simulations were performed and discussed, the iterative fabrication process used to create each component of Starfish is reviewed in detail, and finally, Starfish's ability to securely grasp objects that closely mimic those seen by actual orbital debris in the space environment is tested along with starfish's grip strength on various objects. Starfish demonstrated the ability to passively adjust its grip around target objects due to its extension spring actuated joints, resulting in only a momentary loss of grip strength when a single finger detached from an object before strengthening again. It was determined that Starfish requires 36-40 watts to operate nominally and can perform its capture cycle 45 times before deformation of the structure begins. It was capable of capturing a majority of the debris archetypes that exist in the space environment, performing best at capturing flat plates which comprise 36% of the debris environment and performing worst at capturing spherical objects which comprise 19% of the orbital debris environment.

TABLE OF CONTENTS

ACKNOWLEDGEMENTS.....	i
ABSTRACT.....	ii
TABLE OF CONTENTS.....	iii
LIST OF FIGURES	v
LIST OF TABLES	viii
1 Introduction.....	1
1.1 The History of the Orbital Debris Environment	1
1.2 What is Orbital Debris?	2
1.3 Current Orbital Debris Environment	5
2 Review of the Relevant Literature	7
2.1 Methods of Removing Orbital Debris.....	7
2.1.1 Atmospheric Drag and Graveyard Orbits	7
2.1.2 Magnet Based ADR	8
2.1.3 Grabber Based ADR	9
2.1.4 Tether Based ADR.....	9
2.1.5 Net Based ADR.....	10
2.1.6 Soft Attachment Methods	10
2.1.7 Ground and Space Based Laser Methods	11
2.1.8 Harpoon Based ADR	11
2.1.9 Drag Sail Based ADR	12
2.2 Examples of ADR in Space	12
2.3 Common ADR Shortcomings.....	13
2.4 Shape Memory Alloys	14
2.5 Aerospace Applications	15
3 Methodology.....	17
3.1 Starfish Design.....	17
3.1.1 Biomimetic Finger Design.....	20
3.2 Theory and Simulations	21

3.3	Fabrication	26
3.3.1	Experimental Process	27
3.3.2	Phase One.....	28
3.3.3	Phase Two.....	28
3.3.4	Phase 3	29
4	Results.....	32
4.1	Phase One.....	32
4.1.1	Half Scale Fingers.....	32
4.1.2	Wire Experimentation.....	34
4.1.3	Phase Two.....	36
4.2	Phase Three.....	37
4.2.1	First Full Assembly.....	37
4.2.2	Mechanical Assembly.....	38
4.2.3	First Grip Test.....	39
4.2.4	Issues with First Assembly	45
4.3	Second Full Scale Design and Testing.....	46
4.3.1	Design Changes	46
4.3.2	Second Assembly Testing Results	52
5	Discussions, Conclusions, and Recommendations	58
5.1	Discussion.....	58
5.1.1	First Grip Test Discussion	58
5.1.2	Second Grip Test Discussion.....	59
5.2	Conclusions.....	63
5.2.1	Comparison of Starfish to Current ADR Methods	64
5.3	Recommendations.....	65
6	REFERENCES	67
7	PUBLICATIONS.....	71

LIST OF FIGURES

Figure 1.1 a) An image of a 5mm hole found in Canada Arm 2 after collision with debris in 2021 [9], b) An image of 40cm wide hole made by ~1cm big piece of space debris in 2016 [10].	3
Figure 1.2 A depiction of the debris cloud formed from the 2021 ASAT test [13].	4
Figure 1.3 An ESA graph of cumulative catastrophic collisions over time [3].	5
Figure 1.4 2021 ESA model of trackable space debris in orbit that year [14].	6
Figure 2.1 Depiction of how shape memory alloys work on a material level [42].	15
Figure 3.1 A diagram of Starfish’s components.	17
Figure 3.2 Image depicting how Starfish operates in relation to the shape memory alloys. ..	19
Figure 3.3 Diagram of the tendons in the human hand [50].	20
Figure 3.4 Image of body-to-body spring connections made between each finger component.	21
Figure 3.5 Static structural analysis of a Starfish finger with the three different springs: a.) 1.4 lbs/in, b.)1.1 lbs/in, and c.) 0.95 lbs/in.....	23
Figure 3.6 Temperature versus recoverable strain percentage for Dynalloy SMA wire with a transition temperature of 90°C [51].	25
Figure 4.1. Images of each half-scale design, a.) Version 1, b.) Version 2, c.) Version 3	32
Figure 4.2 An image of iteration 2, threaded with an SMA and manually bent before testing.	33
Figure 4.3 The preliminary full-scale design.	36
Figure 4.4 Images of Starfish moving from its compact to fully extended phase.	37
Figure 4.5 Fully assembled PETG Starfish.	39
Figure 4.6 One load versus time tests for the rubber ball.	40
Figure 4.7 The average of all ten rubber ball tests with standard deviation.	41
Figure 4.8 One load versus time tests for the bike pump.....	41
Figure 4.9 The average of all ten bike pump tests with standard deviation.....	42
Figure 4.10 One load versus time tests for the craft cube.....	42

Figure 4.11 The average of all ten craft cube tests with standard deviation.....	43
Figure 4.12 One load versus time tests for the glass.....	43
Figure 4.13 The average of all ten glass tests with standard deviation.....	44
Figure 4.14 One load versus time tests for the metal cone.	44
Figure 4.15 The average of all ten metal cone tests with standard deviation.	45
Figure 4.16 Examples of two more complex SMA finger designs for prosthetics [53], [54].	48
Figure 4.17 Depicts the three different types of wire configurations used for the finger designs.....	48
Figure 4.18 Image of new finger design.	49
Figure 4.19 Images of fingers at max extension using a.) 0.95 lbs/in, b.) 1.1 lbs/in, and c.) 1.4 lbs/in springs.	50
Figure 4.20 Image of the full second iteration of Starfish.	51
Figure 4.21 A single load versus time test for the spheroid object.....	52
Figure 4.22 The average of all ten spheroid tests with standard deviation.....	53
Figure 4.23 One load versus time tests for the straight rod.	53
Figure 4.24 The average of all ten straight rod tests with standard deviation.	54
Figure 4.25 One load versus time tests for the bent rod.	54
Figure 4.26 The average of all ten bent rod tests with standard deviation.	55
Figure 4.27 One load versus time tests for the bent plate.....	55
Figure 4.28 The average of all ten bent plate tests with standard deviation.....	56
Figure 4.29 One load versus time tests for the flat plate.	56
Figure 4.30 The average of all ten flat plate tests with standard deviation.	57
Figure 5.1 Capture of the straight rod a.) versus the capture of the bent rod b.). The prevention of the fingers from fully closing around the straight rod by the clamp can be seen...	61
Figure 5.2 Image of Starfish at the end of capturing the bent plate. The two left fingers do not have a solid grasp on the object due to the plate pushing them flat while the center and right most fingers have a better grasp.	62

Figure 5.3 Image of the flat plate becoming lodged between multiple joints and beginning to overextend the fingers..... 63

LIST OF TABLES

Table 3.1 SMA values required to accurately model Dynalloy shape memory wire in ANSYS.	24
Table 3.2 Objects used in the first capture test with their weight and dimension specifications.....	29
Table 3.2 Simplified list of orbital debris shapes [20].....	31
Table 3.4 Objects chosen for the second grab test and their dimensions.	31
Table 4.1 Electrical values found during half scale trials for each wire type.	35
Table 5.1 Material composition of orbital debris objects [20].....	65

1 Introduction

Since man's first venture into space, there has been space debris. While originally insignificant in both presence and consequence, the situation has now become increasingly volatile with each passing year. The magnitude of the already present debris is only exacerbated by continuous launches with minimal priority being given to remove any of the debris. If this issue is not mitigated in the near future, space travel will become near impossible due to the constant threat of collision. Various designs for debris removers have been proposed, but very few have actually made it to space, with those that have only capable of removing one target object per mission. However, this is not enough to lessen the consequences of the ever-growing ocean of debris. This section serves to paint a clear image of the current orbital debris environment by analyzing its history, current trends, and just what exactly orbital debris is. This thesis aims to provide a solution to the orbital debris problem by first analyzing the current state of orbital debris removal methods and their shortcomings then designing, fabricating, and testing a new debris remover to overcome these flaws.

1.1 The History of the Orbital Debris Environment

In 1978, Dr. Kessler and Dr. Cour-Palais speculated that physical remnants from past missions could pose serious issues for future space travel and long-term missions if not eventually dealt with [1]. Kessler and Cour-Palais theorized that in the somewhat distant future, the populated orbits above Earth would eventually lead to collisions between two or more objects. This collision would then in turn send the resulting collision debris careening in all different directions where it would impact other objects, creating a continuous cycle of debris generation until all orbits comprise entirely of dense clouds of debris. This destructive cycle would later be called the Kessler Syndrome [2]. Pre-2009 debris was primarily generated from rocket separations [3]. Minor impacts from small debris on operational spacecrafts and satellites

did occur but were not considered to be an overall hazard, as shown in Figure 1.

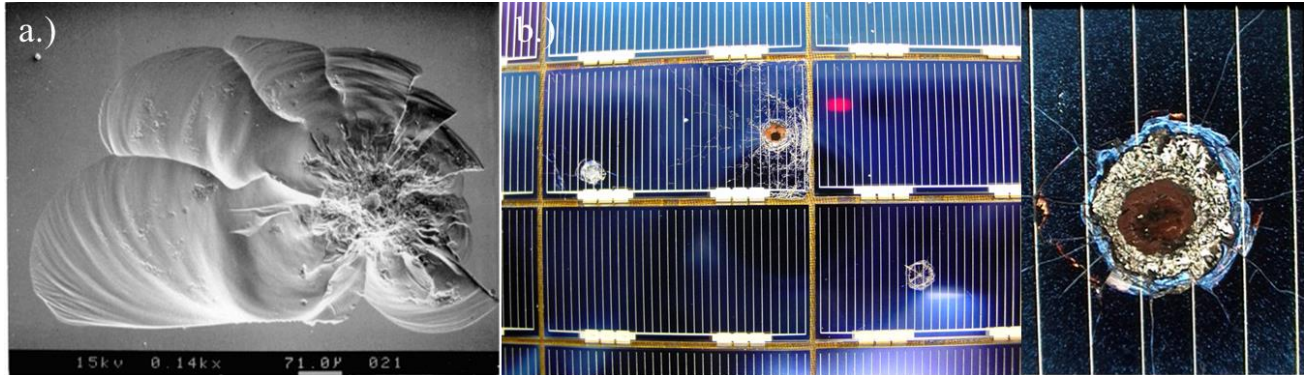


Figure 1.1 a) Image of space shuttle window after debris impact in 1992 [4] and b) image of multiple debris impacts on Hubble telescope solar arrays in 2002 [5].

In 2007, China destroyed one of their own satellites during an antisatellite test (ASAT) creating over 3,000 pieces of fragmentation debris [6]. In 2009, the first ever accidental collision between two satellites, Cosmos 2251 and the operational Iridium 33, occurred; creating roughly 2,269 pieces of debris [6]. These two events alone caused fragmentation debris to become one to one with the previously dominant launch debris [3]. As the years went by, the rate of things being launched into space increased dramatically, increasing not only the amount of debris being generated but the odds for another catastrophic collision to occur as well. In fact, the debris from Feng-Yun 1C caused the destruction of a small Russian satellite, BLITS, in 2013 [7]. In 2021, Russia performed an ASAT test that resulted in another 1,500 pieces of trackable debris to be generated and caused the crew of the International Space Station (ISS) to have to shelter in place [8].

1.2 What is Orbital Debris?

Orbital debris is any rouge object in orbit above Earth that is no longer used for any active space missions. This debris can be as small as a fleck of paint or as large as a discarded rocket body. The European Space Agency (ESA) categorizes orbital debris by its point of origin to help better visualize what casues debris. These categories are: rocket debris, rocket mission related

objects, HAPS fragmentation debris, H8 fragmentation debris, other rocket fragmentation debris, rocket bodies, payload debris, payload mission related objects, Fengyun 1C fragmentation debris, Cosmos 1408 fragmentation debris, Cosmos 2251 fragmentation debris, Iridium 33 fragmentation debris, and other payload fragmentation debris [3]. It can be seen that some of these categories are entirely comprised of fragmentation debris from historical breakups like Feng-Yun 1C and Cosmos 1408. This demonstrates just how long lasting the effects of these incidents can be on the space environment. More generally however, debris is categorized by its size with objects of one meter or larger being dubbed “large” debris and anything smaller than one meter being dubbed “small” debris. The exact size range for each of these categories is highly debated. Some debris is classified as “untrackable”. These pieces of debris are so small that they cannot be picked up by modern tracking equipment. Though small, they pose just as much of a threat to space operations as the trackable pieces do due to their high levels of kinetic energy [2]. Figure 1.2 depicts the effects of these impacts on space structures for this type of debris.

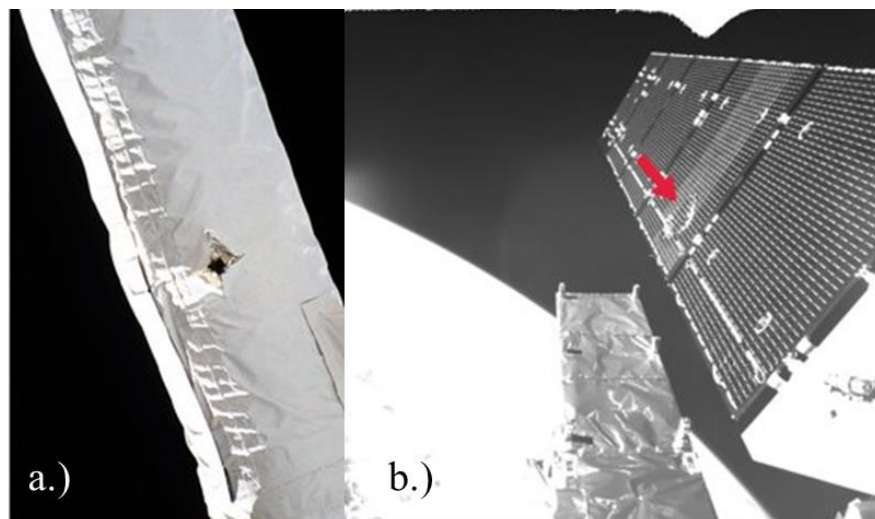


Figure 1.2 a) An image of a 5mm hole found in Canada Arm 2 after collision with debris in 2021 [9], b) An image of 40cm wide hole made by ~1cm big piece of space debris in 2016 [10].

It can be seen that though the debris that impacted these structures were only millimeters large, their velocity at impact created damage areas far greater than their true size. Debris inhabits many different orbits but most commonly populates 500 km at 97.4° inclination, 700km at 98.19° inclination, and 800 km at 98.6° inclination [3]. This is quite worrisome as these orbits are also commonly used by active satellites and other spacecrafts.

Debris tends to travel around 7km/s, and in the case of small debris, travel in large groups called “clouds” [11]. Each piece of debris in these clouds is heavily monitored by multiple government agencies worldwide. NASA keeps an extensive catalog showing every trackable piece of debris in each cloud as well as the apogee and perigee of these pieces [12]. and used to inform satellite owners of when their satellites must perform a collision avoidance maneuver. Performing these maneuvers has become more and more common due to the rising amount of orbital debris. Figure 1.3 shows a depiction of the debris cloud generated from the 2021 Russian ASAT test.

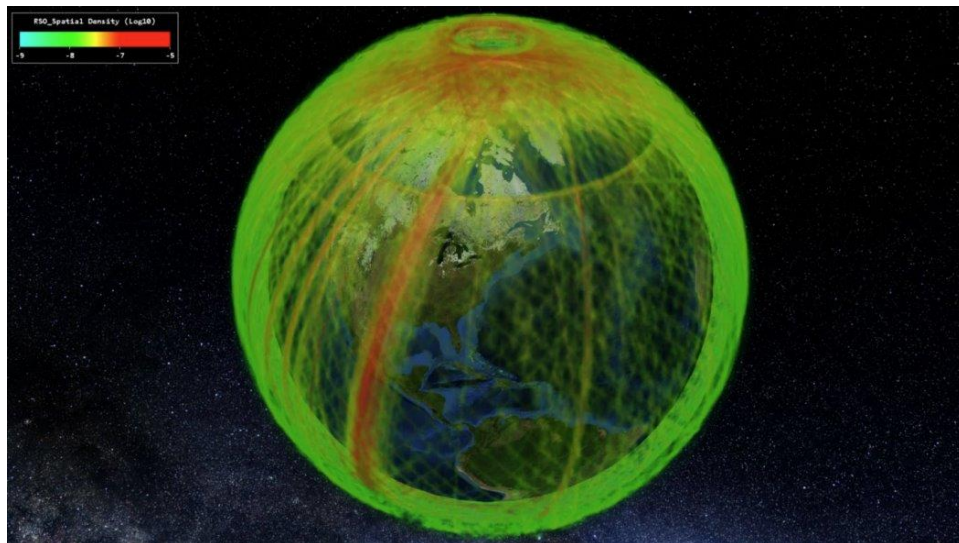


Figure 1.3. A depiction of the debris cloud formed from the 2021 ASAT test [13].

1.3 Current Orbital Debris Environment

Every year the amount of launches that occur surpasses the previous years. With the most recent SpaceX Starlink launch adding 23 more satellites into orbit, this growing trend shows no sign of stopping. Figure 1.4 depicts the current trend of projected catastrophic collisions over time if all space launches were to cease and with the current projected rate of launches extrapolated over time.

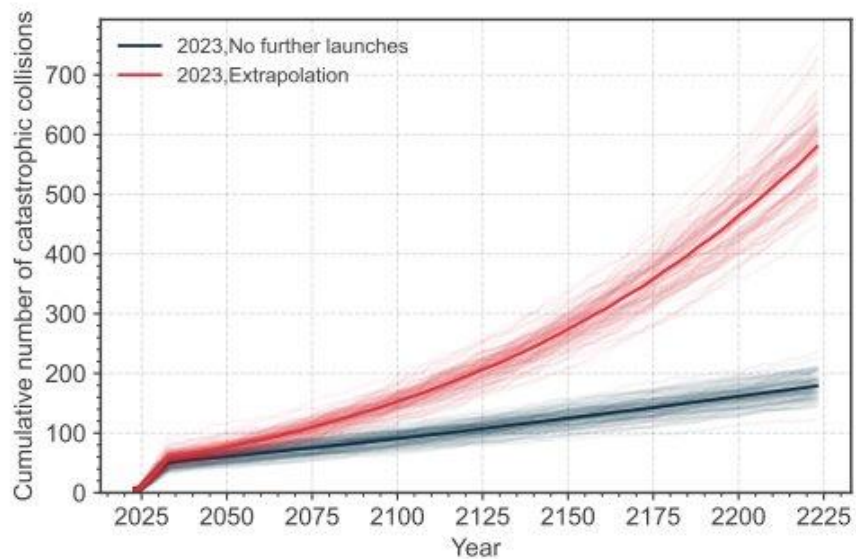


Figure 1.4 An ESA graph of cumulative catastrophic collisions over time [3].

From this graph it can be seen that within the next 25 years just under 100 catastrophic collisions are projected to occur should the current increasing rate of launches continues. While 25 years may not seem like a short amount of time, all it takes is one severe collision to begin the catalytic cycle that is the Kessler Syndrome. While the exact number of debris in each size category is different depending on the nation that reports them, ESA reports that as of 2023 there are 34,000 objects greater than 10cm, 900,000 objects from 1cm to 10cm, and an estimated 128 million objects from 1mm to 1cm in size [3]. The sheer intensity of just how much orbital debris

is present in orbit above Earth can be hard to comprehend, let alone visualize, based on these numbers alone. Therefore, Figure 1.5 has been provided to help do so.

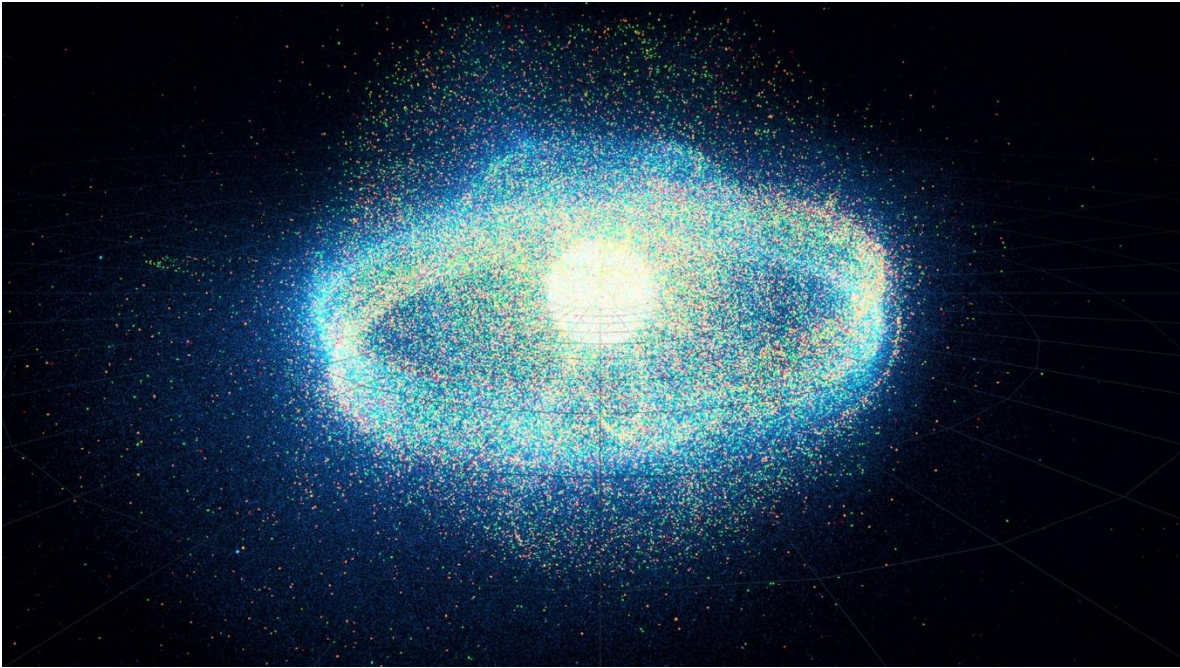


Figure 1.5 2021 ESA model of trackable space debris in orbit that year [14].

In Figure 1.5, every single dot is a piece of trackable debris in orbit above Earth where in the red dots represent objects larger than 10cm, the orange dots represent objects from 1cm to 10cm, the green dots represent objects from 1mm to 1cm, and the blue dots represent objects below 1mm in size. In this figure the densely populated orbits discussed previously can be seen as well. The orbital debris issue is a rapidly growing problem that will have devastating effects on space operations if left untreated.

2 Review of the Relevant Literature

It has been shown that the looming threat of orbital debris is very real and in serious need of attention. Thankfully, there are a few operations that have begun the arduous task of collecting and deorbiting this debris, though they are limited and have not been able to actually remove any debris [15,16]. This section will discuss current active debris removal (ADR) methods that have been tested in a space environment as well as theoretical designs that have been proposed in the past. Political limitations for space debris removal shall also be discussed. A summary of the current challenges in achieving orbital debris removal will be discussed.

2.1 Methods of Removing Orbital Debris

There are two schools of thought when it comes to removing orbital debris: prioritize removing the smaller debris that poses the most immediate threat or prioritize large debris since it is a future threat. Neither approach is right or wrong, but each comes with their own challenges. For example, if one is to focus on removing larger debris, then approximately five large objects a year must be removed to maintain the current debris environment [17]. This means that to actually reduce the presence of large object debris, more than five objects a year must be removed. If one is to prioritize small debris instead then an area of 1000 km^2 of debris needs to be removed every year [17]. A vast majority of ADR designs focus on removing large debris as opposed to small debris, likely because of this difference in how much debris needs to be removed per year between the two categories.

2.1.1 Atmospheric Drag and Graveyard Orbits

Historically, when a spacecraft was no longer needed or had completed its mission one of two methods would be employed for it to be deorbited: letting atmospheric drag take it down if it was close enough to do so or parking it in a graveyard orbit so that it could be dealt with later. Neither of these old school methods are sustainable any more as the graveyard orbits are now full

and letting atmospheric drag take over poses too much of a risk to other active missions unless in very low orbits. Up to certain orbits, atmospheric drag has some influence on the trajectory of objects. This effect causes these objects to be slowly pulled back into Earth's atmosphere over time where they will burn up upon re-entry. This is what causes the ISS and other low orbit spacecraft to have to be reboosted every so often [18]. While not desirable for active missions, atmospheric drag used to play a large role in deorbiting debris. It was initially thought that any debris that resulted from a launch would not be an issue as this atmospheric drag would dispose of it naturally over time. While true in the past, this has become incredibly difficult to rely on due to the growing number of active objects in low Earth orbit. Letting a defunct satellite decay via atmospheric drag now poses the risk of colliding with these active objects and causing a devastating amount of new debris to be generated.

Graveyard orbits are where large defunct objects are left to sit until they can be deorbited in a safe and nondisruptive manner. These orbits are well away from any actively used orbits so that the objects kept withing them will not pose any threat to current space operations. Objects in these orbits are still minimally affected by atmospheric drag and will eventually be pulled closer to Earth again over a very long amount of time, roughly 120 – 200 years [19]. This disposal method is not sustainable as it only serves to put off the removal of these typically larger objects as well as making it very difficult to remove them due to their distance from the Earth. Any mission intended to deorbit the debris in these orbits would have to expend a lot of energy just to get to them as well as make the journey back to Earth with these objects in tow.

2.1.2 Magnet Based ADR

In this ADR technique, a design with a magnetic component is used to capture debris. This component works like a docking mechanism and allows for the satellite chasing the debris (often referred to as just the “chaser”) to maintain a strong hold on it once close enough to make

contact. This ADR method was one of the few actually tested in space via Astroscales ELSA-d servicer satellite [16]. ELSA-ds magnetic docking system did prove successful in capturing a practice target but is only compatible with satellites that have the corresponding docking port. Many theoretical designs include the use of a magnetic component as support to an additional ADR method, such as tethers. These designs do have a major flaw however, they are limited to only capturing debris made of magnetic materials, which comprise only 4% of the orbital debris environment [20].

2.1.3 Grabber Based ADR

These ADR designs rely on a classic “claw” style grabbing method wherein multiple actuated rigid structures wrap around a piece of debris. These are often actuated via motor or solenoid systems and can be either attached to a robotic arm or directly attached to a chaser satellite. The claws can consist of one, two, or multiple arms to assist in the capture of a target [21]. These arm structures can also be non-rigid and capable of wrapping around targets, referred to as tentacle grabbers [22]. This type of ADR method is typically limited to orbital debris in certain size categories which depends on how small of an object the claw itself is designed to grab. An additional issue is that if a robotic arm system is being used, the chaser satellite connected to the arm runs the risk of destabilizing when capturing tumbling debris [23]. This method is typically used for larger orbital debris such as rocket bodies. The Clearspace-1 mission for example, intends to capture a part of a Vespa rocket though the launch date continues to be pushed back [24].

2.1.4 Tether Based ADR

This method of ADR requires either a cable or ribbon-like tether to be attached or brought close to a target piece of debris in order to deorbit it via towing or electrodynamically. Tow tethers connect the target debris to the chaser so that it can be physically pulled out of orbit [25].

This method is assisted by the increase in the debris' overall surface area from being connected to the chaser, causing it to be more influenced by atmospheric drag and deorbit faster. In the case of electrodynamic tethers, a magnetic field is used to “influence” targets back into the atmosphere without physically interacting with them [26]. Some challenges with this type of remover are that they are difficult to test in atmosphere and are less reliable in capturing debris since they are mostly contactless [23]. This design is also meant for larger to midsize pieces of debris as it becomes increasingly difficult to attach a tether to smaller pieces of debris. One example of this type of remover is the University of Madrid's E.T.Pack, an electrodynamic tether intended to launch in 2025 [27].

2.1.5 Net Based ADR

This method requires a chaser satellite to match speeds with a target piece of debris so that it can launch a large net at it. This design is more dynamically complex than the other ADR methods as the launch of the net and capture of the target result in damaging oscillation effects on the chaser satellite [23]. This method has the advantages of being able to capture targets from a distance, not requiring the chaser and target to dock in any way and can capture debris of various shapes and sizes [28,29]. However, the nets in these designs can be difficult to deploy and control. They can also only be launched once or twice per mission before having to be deorbited due to the complexity of redeploying the net [23]. This creates a serious risk of mission failure should the net miss its target.

2.1.6 Soft Attachment Methods

“Soft attachment methods” is an umbrella term for many forms of ADR that capture debris in a gentler fashion. Examples of this include electrostatic, chemical bonding, adhesives, and Van der Waals capture techniques [30,31,21,32]. While different in technique, these methods all follow the same routine during capture. The chaser approaches the target debris and softly makes

contact with it while activating its attachment method. This creates a somewhat solid bond between the target and chaser. These techniques usually require a lot of power to maintain their hold on the target in the case of electrostatic and chemical bonding or lack durability in the case of adhesives and Van der Waals methods since the materials necessary to maintain their grip decay rapidly in a space environment [23].

2.1.7 Ground and Space Based Laser Methods

By far the most controversial method of ADR removal is the laser-based method. This method utilizes one or more powerful lasers to deorbit debris via ablation [33]. This method requires incredibly precise tracking systems, a large amount of power, and the ability to cover a wide area to be capable of deorbiting debris [21]. This method has never been implemented due to many political entities' fears of it being used for purposes other than debris removal, though many concepts have been proposed [21,34]. While the technology to implement this ADR method does exist, there are too many drawbacks and barriers for it to ever leave the conceptual stage.

2.1.8 Harpoon Based ADR

Similar to net based methods, this technique also requires a chaser craft to match speed with a target object. Once done, the chaser will launch a harpoon that shoots through the target object and is then reeled back to the chaser craft or towed back into the atmosphere [35,36]. This technique is also rather controversial due to the damage it causes to the target object, which can result in more pieces of debris being generated from fragmentation or full breakup of the target [23]. This method is also occasionally limited to the amount of time it can be launched per mission depending on the method used to launch it, as seen during the test of the RemoveDebris mission [15].

2.1.9 Drag Sail Based ADR

In this ADR method, a large sail is attached to a piece of debris. This results in a significant increase in the debris' overall surface area, causing atmospheric drag to deorbit the target at a much faster rate than normal [33]. This concept has the advantages of being affordable and easy to test on the ground, so many concepts have been proposed [37]. These sails are typically deployed using large, extendable booms that are either mechanically operated or inflated [37,15]. This method takes up a large amount of space which can increase the risk of colliding with other objects as it deorbits [33].

2.2 Examples of ADR in Space

Many of the previous ADR techniques have only ever been discussed theoretically or remain at low technology readiness levels (TRL). Very few have ever actually been tested in space and of those few, none of them have been able to remove an actual piece of debris from the environment.

ELSA-D is a magnet based orbital debris remover launched in 2021. It deorbits end of life satellites by magnetically docking with them via a matching docking plate. ELSA-d then lowers itself to an orbit where it will be eventually pulled back into the atmosphere with the attached target where both will be burned up upon re-entry [16]. As previously mentioned, ELSA-d can only deorbit satellites with the corresponding magnetic attachment, which no piece of orbital debris has. Additionally, ELSA-D can only deorbit one object per mission [16].

Another orbital debris remover that made it to space testing is RemoveDebris in 2018, which included a net, harpoon, camera, and drag sail. All of these methods were demonstrated on pseudo-targets that were brought up with RemoveDebris upon launch [15]. The net, harpoon, and camera were all successful in their ability to locate and/or capture these mock targets but the drag sail did fail to deploy due to a leak in its inflatable boom [15]. After capturing these targets

RemoveDebris was left to passively deorbit back into the atmosphere and was confirmed to have burned up in 2021.

Clearspace-1 intends to be the first ever orbital debris remover to actually remove a piece of debris from space. However, its launch date has been pushed back from 2025 to 2026 due to a piece of orbital debris colliding with its intended target in August of 2023, causing it to fragment [38]. This event further demonstrates the immediate need to prioritize removing orbital debris before more can be generated.

2.3 Common ADR Shortcomings

From this literature review of current and prospective ADR methods, some reoccurring flaws can be seen. Firstly, nearly all ADR methods both proposed or implemented can only capture, at most, one piece of debris per mission and are not reusable as they are meant to burn up upon re-entry with their target. As has been previously determined, at least five large objects per year need to be removed in order to maintain the current environment. Therefore, all of these ADR methods would need to be built and launched five times in a year, assuming each launch results in a successful capture. However, this number of successful captures per year will only increase as time goes on due to the rapidly increasing rate of objects being launched every year. Again, this is only if the goal is to maintain the current environment, not improve it. This entire system would be incredibly expensive to maintain due to the continuous manufacturing of a specialized debris remover each launch and the costs of five launches a year at minimum. Additionally, a large number of these ADR methods also come with a high chance of mission failure or the risk of generating more debris in the process of removing just one target. Almost all of these ADR methods are limited to only being able to capture orbital debris of specific materials and sizes. Finally, all ADR methods discussed here are meant to capture debris 10cm in size or larger. Consequently, that means that there are no current methods for capturing objects that are in the

1cm to 10cm category, of which there are nearly one million. While it is beneficial to remove the larger debris that have the highest risk of generating more debris should they collide with another object, it is equally as important to remove the debris that causes the most immediate threat to current space operations. This is evident given the amount of impacts on operational spacecrafts by small debris as well as the effects they can have on current debris. An impact from an untrackable piece of debris was enough to fragment a Vespa rocket stage and may result in the end of the Clearspace-1 mission meant to remove it.

Based on these shared short comings between the current ADR methods, an optimal orbital debris remover should have the following qualities: it must be reusable so that it can capture more than one object per mission, must not be limited by the shape or material of a piece of debris, be rapid to manufacture and cost effective, and have minimal points of mechanical failure. Some additional requirements that would increase the effectiveness of an ADR method are being compact so that multiple can be carried up per launch, low power requirements to help it be reusable more times in one mission, and has minimal points of mechanical failure in order to reduce the odds of mission failure.

2.4 Shape Memory Alloys

The shape memory effect was first discovered in gold-cadmium alloys by the Swedish scientist Arne Olander in 1932 [39]. It was not until 1959 however, that the most commonly used shape memory alloy (SMA), Nitinol, was first discovered by the United States Naval Ordnance Laboratory [39]. Due to its many advantageous properties, Nitinol is now used in a variety of fields including biomedical, robotics, and aerospace. Shape memory alloys like Nitinol allow complex mechanical systems to be simplified due to their high actuation forces, high power to weight ratio, reliability, compactibility, and high number of activation cycles [40]. These properties are a result of SMAs material composition. SMAs have the ability to transition

between two crystalline phases, austenite and martensite. When heat is applied to an SMA it causes it to shift from the low temperature martensite phase to the higher temperature austenite phase due to the atoms rearranging to form the new phase's crystalline structure [41]. Figure 2.1 illustrates this phase change.

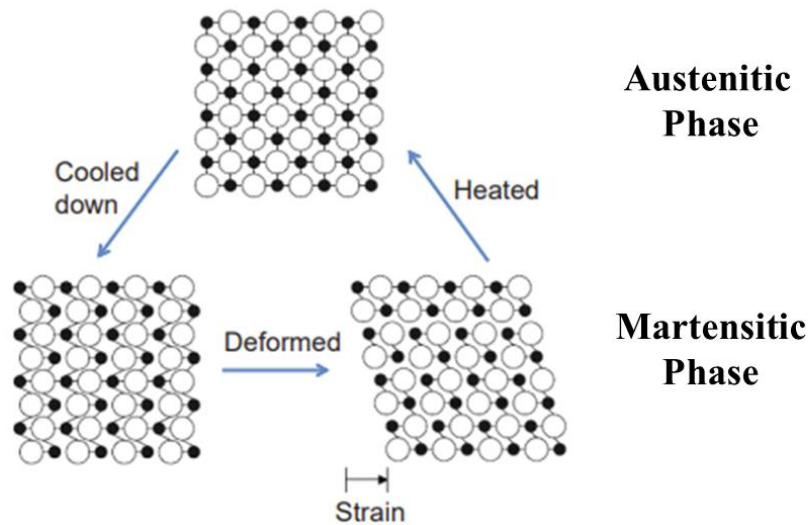


Figure 2.1 Depiction of how shape memory alloys work on a material level [42].

The temperature at which this shift begins is referred to as an SMA’s transition temperature. This phase change allows for SMAs to be trained to “remember” certain configurations in their austenite phase. Meaning, an SMA can be deformed and strained while in its martensite phase but when heated to its transition temperature will return to its originally trained form. At this stage, the SMA material recovers the strain acquired during its martensite deformation and becomes difficult to deform. When this heating is stopped, the SMA becomes less stiff as it gradually returns to its martensite phase and can be deformed once again.

2.5 Aerospace Applications

There are numerous examples of SMAs being used in the Aerospace industry for both air and spacecraft. Firstly, SMAs were experimented with to solve the issue of efficiency of aircraft inlets during flight. The Smart Aircraft and Marine Propulsion System demonstration

(SAMPSON) used SMAs to create and test variable inlets for the F-15 aircraft [43]. This demonstration used a system consisting of SMAs and other smart materials to actuate the compliant surfaces on the F-15 intake during different stages of flight to determine if intake efficiency could be improved. Testing of this variable inlet was performed in the high-speed wind tunnel at NASA Langley. A second example of SMAs being used for morphing aircraft structures is the Variable Geometry Chevron that was flight tested by Boeing. Chevrons are located on the trailing edge of aircraft engines and are primarily used to reduce noise during takeoff [40]. However, they can also cause an increase in drag during cruise. To fix this, researchers at Texas A&M university created the Variable Geometry Chevron system that uses Nitinol composite beams to actuate the chevrons during flight [44]. This system was tested both in flight on a Boeing 777 and during a static engine test in 2005 [45].

One in space use for SMAs are as washers for vibration control of cryocoolers [46]. The properties of the SMA washers allow the vibrations that cryocoolers experience during launch and mission activities to be minimized. SMAs are also used as low shock release devices for solar panels and other deployable payloads [47]. Here slower actuation of the SMAs allows for smoother deployment of payloads and solar arrays, preventing them from facing the high shock that would normally be felt if standard methods were used. SMAs are also currently in development for long term space missions as wheels for future rovers [48]. The wheels of rovers are subject to harsh surface conditions that result in large amounts of wear and tear on their wheels. SMA mesh wheels would allow the tires of rovers to adapt and conform to the harsh surface conditions and minimize the degradation of the wheels.

3 Methodology

The proposed design of this thesis, Starfish, will be introduced and relevant research to justify the design of Starfish will be analyzed. The ideal ADR requirements established in chapter two were used as the foundations for designing Starfish.

3.1 Starfish Design

Starfish aims to use a combination of shape memory alloys and extension springs to capture debris in a low power and reusable way that is not limited in the types of debris it can capture. It is meant to capture debris 15cm in length or smaller. Starfish is capable of being compacted into 1U so that many can be brought up during one mission. This would allow for multiple pieces of debris to be removed in one mission rather than just a single piece. Due to its low power design, Starfish requires only 36-40 Watts to operate effectively.

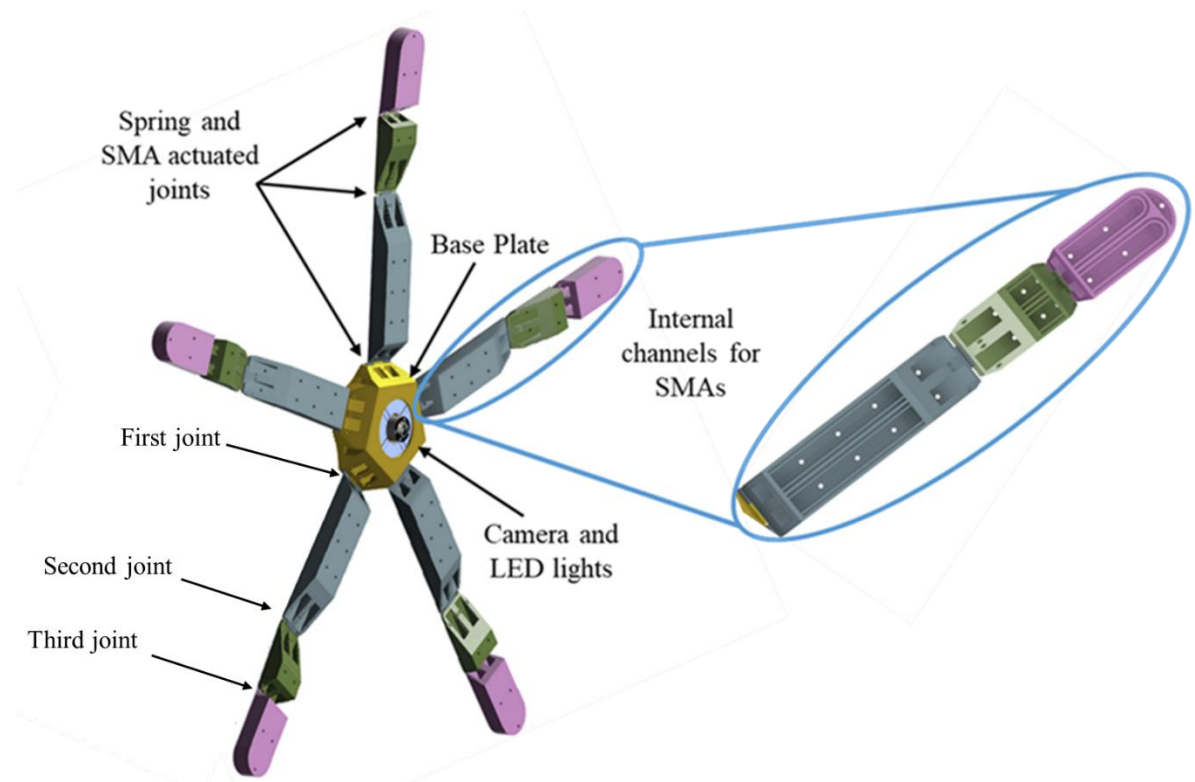


Figure 3.1 A diagram of Starfish's components.

From this literature review it is clear that while there are many variations in ADR designs, there are also many common flaws among them. Thus, this thesis aims to build an orbital debris remover without these flaws to finally begin the debris removal process before it's too late. Figure 3.1 depicts Starfish, the proposed orbital debris remover. Starfish was chosen to be a claw style ADR method since this technique has the most versatility when it comes to capturing different types of debris. Shape memory alloy wires and extension springs are used in place of motors to mitigate the main flaws of the claw style. The shape memory alloys are threaded through each of the five finger like structures of Starfish. The finger structures themselves are segmented into three separate bodies shown in blue, green, and purple in Figure 3.1. These body segments are connected to each other via hinges and are pulled together using two extension springs between each body. This causes Starfish to naturally be in a closed and compact shape. The compact form dimensions of Starfish are 9.2cm in height, and 7.1 cm in diameter. This size makes it easy for Starfish to fit within a single 1U cube satellite, allowing for multiple Starfish devices to be deployed in one launch.

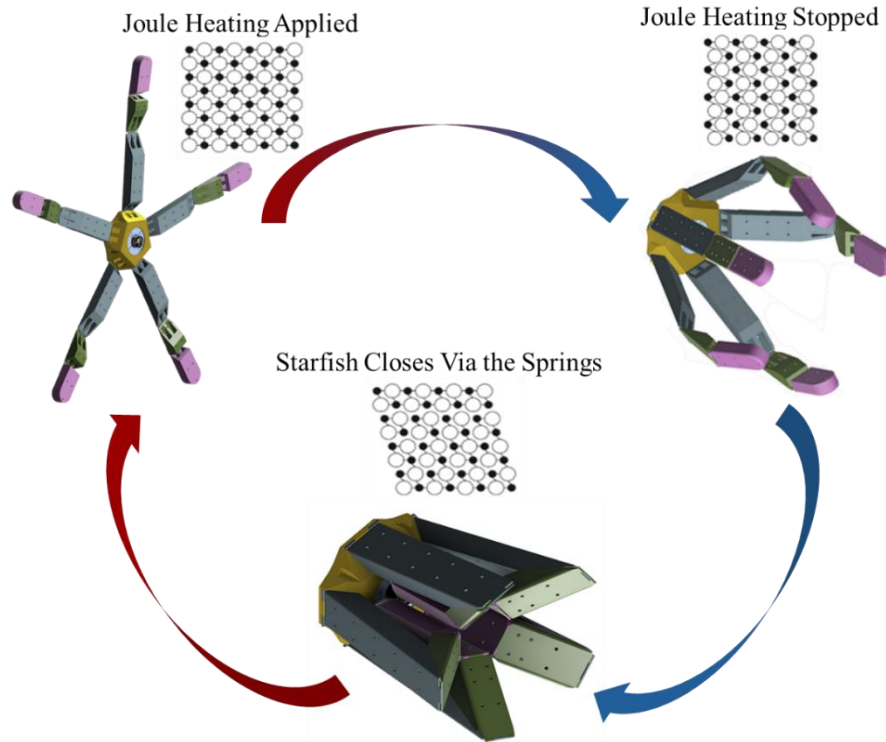


Figure 3.2 Image depicting how Starfish operates in relation to the shape memory alloys.

Once deployed, the SMA wires threaded throughout Starfish activate as shown in Figure 3.2. The SMAs in Starfish are trained to straighten when heat is applied. Therefore, when Starfish is in its compact stage, the wires are deformed. When Starfish begins to approach a debris target, power is supplied to the SMA wires, causing them to heat up via Joule heating. Once the wires reach their austenite transition temperature, they will begin to straighten, causing the fingers to fully extend. At this point, Starfish can be maneuvered within capture range of the target via the cube satellite it is attached to. Once capture is ready to be initiated, power will be disconnected from the SMAs, causing them to cool down and become less stiff. At this point, the pulling forces from the extension springs will overcome the stiffness of the SMA wires and pull Starfish's fingers closed around the target. This is anticipated to create a substantial amount of grip on the target as the extension springs will want to return to their equilibrium position,

causing the grip to tighten around the target. Additionally, due to the high fatigue limit of SMAs and anticipated low power requirements, this capture process can be repeated multiple times in a mission if Starfish misses or does not securely capture a target. As Starfish begins to deorbit using a mechanism such as D3 [49], any movement of the target within Starfish's grasp will only cause a stronger grip to occur. This is because any free space created within the range of Starfish's grip will cause the extension springs between each joint to contract further, reaffirming its grip on the target. Once Starfish re-enters Earth's atmosphere, it will burn up along with the target debris, eliminating it from the debris environment. If more than five Starfish devices are deployed per launch, a substantial dent can be made in the orbital debris environment every year.

3.2 Biomimetic Finger Design

It has been determined that the claw/grabber-based ADR technique demonstrates the greatest potential in being the most optimal ADR technique, as they already meet the most qualifications. In the search for ways to use this technique to meet all set qualifications, it was decided that the most common claw/gripper of all time be used as the foundation for Starfish: the human hand.

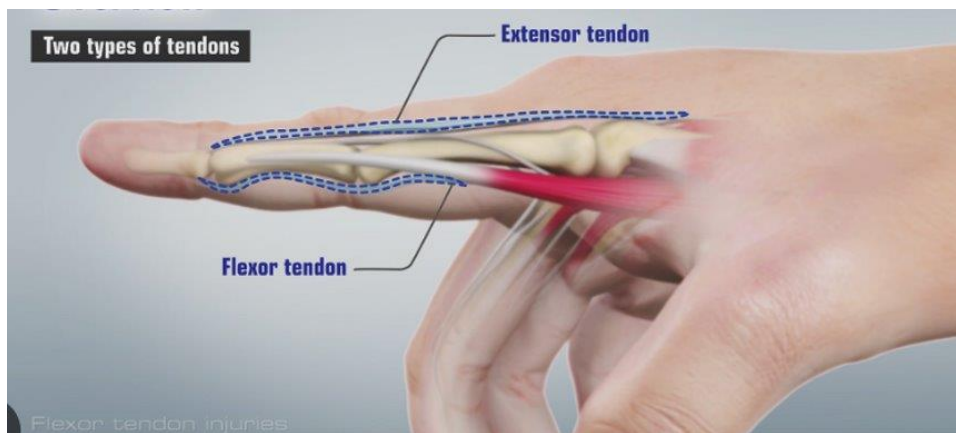


Figure 0.1 Diagram of the tendons in the human hand [50].

The layout and purposes of all three major components that comprise Starfish are meant to replicate the basic functions of the human hand shown in Figure 3.3. The shape memory alloys act as extensor tendons, which are located on the backside of fingers and are what allows them to

extend. The extension springs, located on the inner side of each joint, operate as flexor tendons, which are located on the inside of the human hand. Finally, the hard outer shell of the fingers acts as the bone that the tendons attach themselves to. This biomimetic layout will allow Starfish to be able to passively adjust its grip due to the natural state of Starfish being its compact form. The springs will want to close regardless of what is preventing them from doing so, allowing for an object to be gripped tightly. When an object shifts in any way that allows the fingers to constrict tighter around it, they will do so naturally, allowing for a stronger grip to be applied.

3.3 Theory and Simulations

The first simulation performed focused on verifying the required strength of the springs between each joint. The springs needed to be strong enough to snap the joints closed and provide adequate strength when the fingers must maintain a firm grip on a target. However, they must also be weaker than the heated SMAs in order to allow the fingers to fully extend. A simplified model of a finger assembly was imported into ANSYS for this spring analysis. As can be seen in Figure 3.4, pegs representing the screws used to hold the springs in place were used to increase the accuracy of the simulation.

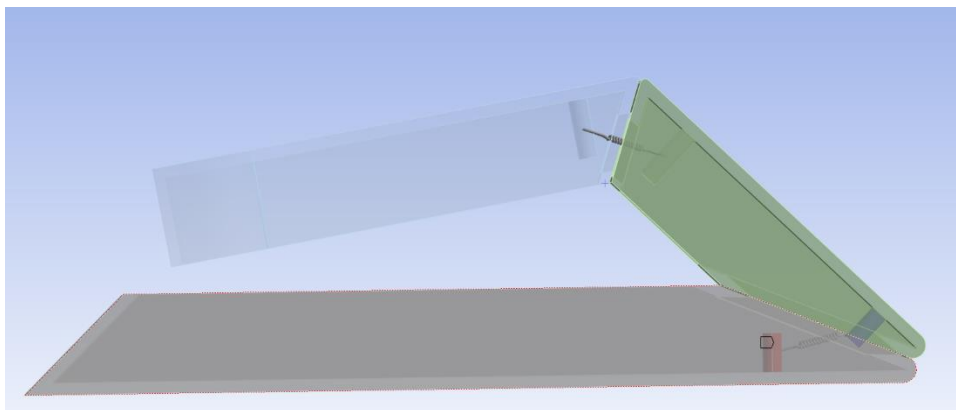


Figure 0.2 Image of body-to-body spring connections made between each finger component.

As PETG was not a material included in the ANSYS library, it had to be manually created. After adding this material to the ANSYS library, each of the labeled body components were assigned as PETG. Four body to body spring connections were then made between each of the pegs, as shown in Figure 3.4. The finger was initially simulated fully closed so that ANSYS would recognize that the springs were in their equilibrium position at this phase and experiencing minimal stresses. A new coordinate system was made in place of the autogenerated global coordinates to ease the interpretation of the resulting force vectors of the simulation. A fixed support was placed on the bottom surface of body one to ground the finger. Frictionless supports were placed on either side of bodies two and three to keep their movements in plane. Rotational connections were made on the fillet edges connecting bodies one to two and two to three. With all supports defined, a displacement moving bodies two and three until they were fully extended was applied. This was done to determine the forces required by the springs to fully extend the finger. Four spring probes were used to determine the forces of each spring at full finger extension. This simulation was performed for three separate spring stiffness values, 1.4 lbs/in, 1.1 lbs/in, and 0.95 lbs/in. The results of each simulation are shown in Figure 3.5 below.

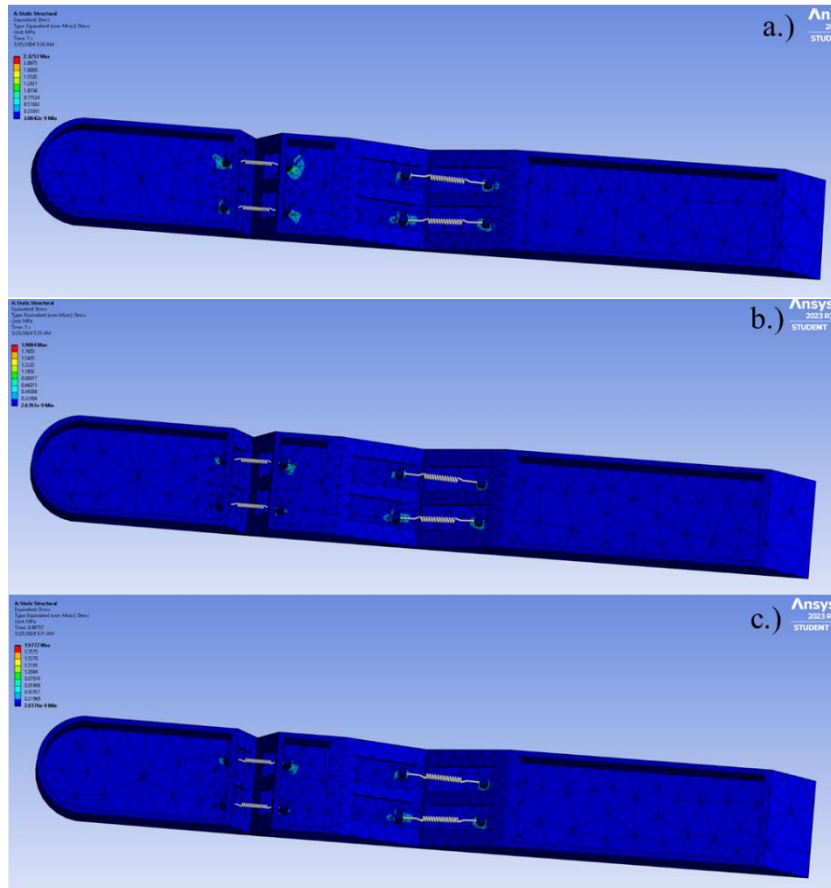


Figure 0.3 Static structural analysis of a Starfish finger with the three different springs: a.) 1.4 lbs/in, b.) 1.1 lbs/in, and c.) 0.95 lbs/in.

From these figures it can be seen that the 0.95 lbs/in spring requires the least amount of force to fully extend the finger. The next simulation that was run was to determine the heat generation of the wires at the required electrical inputs. At this point in the process, the exact length of SMA wire needed and its corresponding power inputs were already experimentally determined. However, the amount of heat generated by the wire at these conditions was unknown. Knowing this would influence future material choices for the finger structures and necessary insulation methods as well as determine max time the fingers can be subjected to this heat before the finger material fails.

For SMA analysis in ANSYS, the following values are required:

Table 3.1 SMA values required to accurately model Dynalloy shape memory wire in ANSYS where “X” denotes a required value that was not provided.

Variable	Symbol	Value
Starting Stress	σ_s^{AS}	X
Final Stress	σ_f^{AS}	X
Starting Stress	σ_s^{SA}	X
Final Stress	σ_f^{SA}	X
Hardening Parameter	h	X
Reference Temperature	T_0	22°C
Elastic Limit	R	X
Temperature Scaling Parameter	β	X
Maximum Transformation Strain	$\overline{\varepsilon}_L$	4.5% [51]
Martensite Modulus	E_m	28 GPa [51]
Austenite Modulus	E_A	83 GPa [51]
Lode Dependency Parameter	m	0

Most of these values are not provided by the manufacturer of the SMAs used in the Starfish experiments. However, the provided values can be used to mathematically derive the needed values to perform accurate simulations. The materials properties given in Table 3.1 are the only ANSYS required values provided by the manufacturer. Figure 3.6 shows how the 90°C wires respond at varying temperatures, which was used to estimate the phase transition temperatures of the wire for calculation.

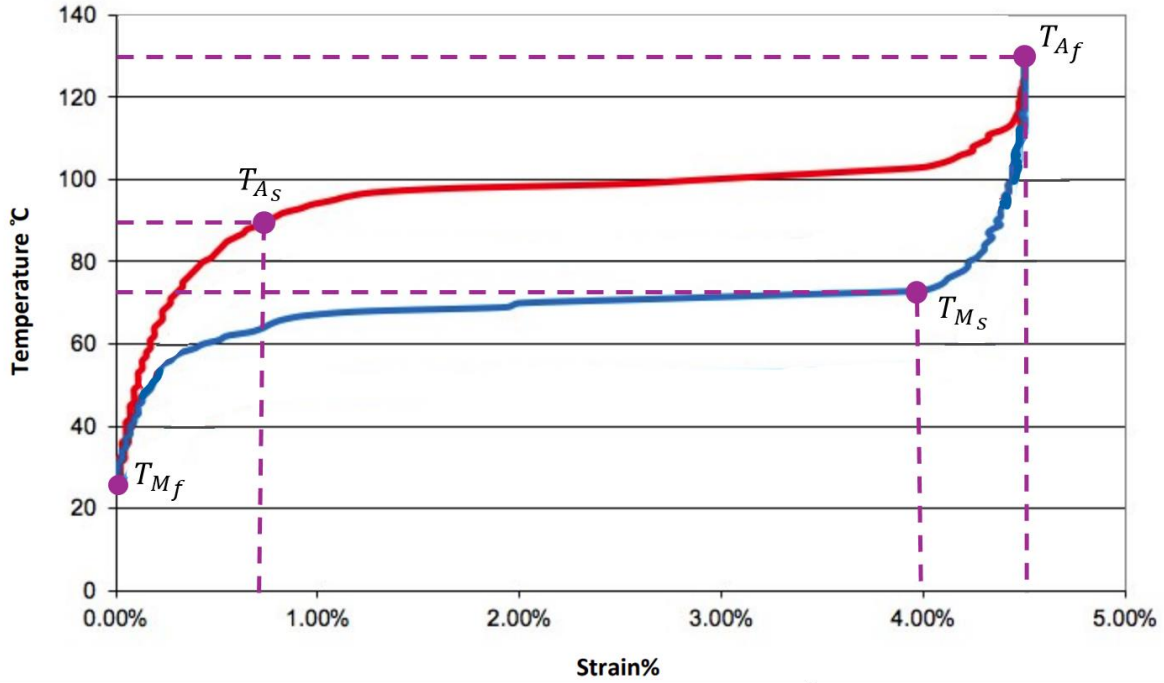


Figure 0.4 Temperature versus recoverable strain percentage for Dynalloy SMA wire with a transition temperature of 90°C [51].

The relationship between the temperature of an SMA and how much stress it experiences is commonly represented using Brinson's model for shape memory alloys [52]. Multiple values required to use this model however are not provided in the Dynalloy wire datasheet and thus a different approach must be taken. Upon further investigation from other literature that also had to derive the stress values from the given Dynalloy data, it was decided that the stresses could be calculated from the thermal stress equation. Where the change in temperature was from one of the known points to the next, each phase's thermal expansion coefficient was used for its respective phase, and the initial stress from one point to another was the previously calculated stress. From the variables that were known or were interpolated from Figure 3.6, the equation for determining thermal stresses in a beam could be used.

$$\sigma = \alpha E \Delta T \pm \sigma_0 \quad (\text{Eq.1})$$

Stresses at each of the phase transition temperatures were calculated starting from the martensite finish temperature and calculating clockwise, adding, or subtracting the previous temperatures stress as needed. Research of other literature that used Dynalloy wires during experimentation showed that a similar approach was taken in order to determine the stress values for simulations. Once these stresses were determined, the other three missing values were found using equations provided by ANSYS:

$$h = \frac{2}{3} \left(\frac{\sigma_f^{AS} - \sigma_s^{AS}}{\varepsilon_L} \right) \quad (\text{Eq.2})$$

Where,

$$\varepsilon_L = \sqrt{\frac{2}{3} \varepsilon_L} \quad (\text{Eq.3})$$

$$R = \sqrt{\frac{2}{3} \frac{(\sigma_f^{AS} - \sigma_s^{SA})}{2}} \quad (\text{Eq.4})$$

$$\beta = \frac{\sqrt{\frac{2}{3} \frac{(\sigma_s^{AS} + \sigma_f^{SA})}{2}}}{(T - T_0)} \quad (\text{Eq.5})$$

The final value m was assumed to be zero as no differences in Young's modulus for tension and compression were given.

With these values, an accurate simulation of the shape memory wires could be created. To begin, a CAD of the wire in a single finger was created with correct dimensions. This model was then imported into ANSYS where a static structural analysis could be conducted.

3.4 Fabrication

Fabrication of the finger shells was done using three different materials. For the initial phases of design and experimentation, the shells were created using 3D printed polylactic acid (PLA)

using equipment from the Embry-Riddle Makers Space. This initial fabrication phase required many rapid iterations of finger shells to be produced, making PLA a useful material as it can be quickly printed and is compatible with all standard 3D printers. After finishing the testing conducted in this phase, it was determined that a more heat-resistant material would be needed to make a full Starfish model. Therefore, a photocure resin was used via a digital light processing printer (DLP) next. These shells performed better than the PLA iterations but ultimately also failed due to the consistent exposure to heat. Finally, polyethylene terephthalate glycol (PETG) was used due to its high melting point of 260°C. The parts for the first full model of Starfish were made using PETG components printed by the universities EPPL lab. However, all iterations after this were done in house using a recently gained PRUSA 3D printer.

3.5 Experimental Process

Experiments were conducted at every step of the fabrication process to optimize the design. By the end of this process, full Starfish iterations could be made using a combination of the best of the available materials. This lengthy process was broken up into three main phases; the first phase consisted of preliminary design, experimentation, and optimization of materials being used. Half scale models were fabricated to test the functionality of the jointed design and determine which shape memory wires had the most ideal qualities. Phase two consisted of fabricating and testing with full-scale finger models, focused on optimizing the physical finger shells and their interactions with the shape memory wires to an achieve an optimized full-scale Starfish by the end. Phase three consisted of testing the grip strength, power requirements, grabbing capabilities, and cycling of this full assembly. Some aspects of this full design were changed to improve issues that arose during testing and a final Starfish model was created and subjected to these same tests again.

3.6 Phase One

This phase began by modeling and printing half-scale fingers to expedite the design process by eliminating or adjusting any basic design flaws. This included things like wire and spring placements, optimal fastener locations, and proper dimensions. Printing the half scale models was also faster than printing and testing full scale fingers and testing them for the same flaws.

While it is common when using shape memory wires to train them to remember a more complex shape for them to function within a design, Starfish only requires them to maintain their manufacturer trained shape of being straight. Therefore, trained wires were deemed not necessary for the design of Starfish though trained wires were used briefly in a later experiment. Three different types of shape memory wires were acquired to experiment how their properties affected their power requirements, abilities to open a half scale finger, and response times. The three wire types chosen varied in both diameter and transition temperature; 90°C with 0.5mm diameter, 80°C with 0.5mm diameter, and 80°C with 1mm diameter. These three wires were chosen knowing that a higher transition temperature would be needed so as not to be easily affected by ambient temperatures in space.

3.7 Phase Two

After the basics of the design were determined, full scale fingers were printed and tested. This phase focused heavily on optimizing the finger design until all flaws were mitigated or fully eliminated. For example, the uses of separate hinges were changed in favor of built in hinges as the shape memory wires would sometimes make contact with the hinges, effecting the power intake and causing the hinges to heat up, also effecting the finger material they were attached to. Issues with the opening and closing of the second joint first materialized at this stage and would

continue to manifest in various ways throughout the following iterations. The material used for the design was experimented with as PLA proved to have too low of a melting point. The two materials experimented with in place of PLA were a photocured resin and PETG because of their higher melting points. Fingers of each material were printed and assembled. Then both were tested at the same power inputs as the PLA fingers to observe if any structural failures occurred.

3.8 Phase 3

This phase consisted of implementing the design changes from phase two to fabricate and test a full Starfish assembly. For grip testing, an Ametek force measurement machine was used. Starfish was fixed to the bottom clamp of the machine while five different objects of varying size, shape, material, and weight were fixed to the top clamp. The objects chosen were picked to test Starfishes ability to capture basic geometric shapes, objects with different textures, and to demonstrate other potentially useful capabilities of Starfish, such as the capture of fragile materials and heavy objects. These chosen objects and their geometrical properties are compiled into Table 3.2.

Table 3.2 Objects used in the first capture test with their weight and dimension specifications.

				
Rubber Ball	Bike pump	Styrofoam Craft Cube	Glass Vase	Metal Cone
12cm diameter 45.02 g	28.3cm long 3.5cm diameter 80.87 g	10cm x 10.3cm x 7.3cm 26.56 g	15.1cm long 5.9cm diameter 159.54 g	15.3cm long 8.1cm largest diameter 70.58 g

The objects chosen were as follows: a stiff foam cube, a metal cone, a small glass vase, a bike pump, and a large rubber ball. These objects were chosen based on their wide array of differences in order to determine which type of targets Starfish would be the best at capturing. Each of the five objects had a metal tab adhered to it via super glue so that it could be fixed to the Ametek force measurement machine's upper clamp. Once a secure grip had been established by Starfish, the force measurement machine would pull the object up at a rate of 100mm/min and collected 100 data points per test. The test would conclude once the object fully broke free of Starfish's grip and the test was repeated 10 times per object.

Based on the results of this test some modifications were made and the finger design was revisited. Some smaller experiments with the wire layout and variation of the extension springs within the fingers took place to eliminate the continuing issues at the second joint. Once this was completed a new full assembly of Starfish was created and tested again.




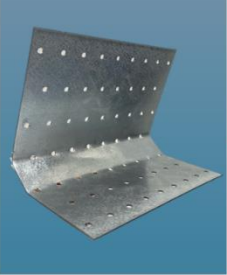
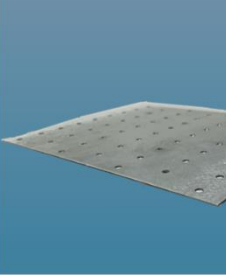
For the second full scale test, the objects chosen were picked to both accurately model real debris shapes that were determined in the paper "An Approach to Shape Parameterization Using Laboratory Hypervelocity Impact Experiments" by Seago Et al. This paper was able to classify five of the most common orbital debris shapes which were; flat plates, bent plates, "nugget" shapes, cylindrical pipes, and bent pipes. These shape archetypes were determined from the results of the DebrisSat experiments conducted by the Department of Defense and NASA's Orbital Debris Program Office. The objects chosen for the second full scale test were chosen based off of their corresponding shape category as well as from real materials that space debris could comprise of which has been compiled in Table 3.3 below. The same grip test was then performed again with these new objects and Starfish design.

Table 3.0 Simplified list of orbital debris shapes [20].

SOCIT4 / Transit	%	DebrisSat	%	Simplified
<ul style="list-style-type: none"> Flat Plate (1%) Flake (13%) 	14%	<ul style="list-style-type: none"> Flat Plate (36%) 	36%	Plate
<ul style="list-style-type: none"> Curled Plate (1%) 	1%	<ul style="list-style-type: none"> Flexible (1%) Bent Plate (2%) 	3%	Plate (Bent)
<ul style="list-style-type: none"> Box (0.3%) Sphere (<0.1%) Box & Plate (<0.1%) Nugget (59%) Other (23%) 	83%	<ul style="list-style-type: none"> Parallelepiped/nugget/spheroid (19%) 	19%	Nugget
		<ul style="list-style-type: none"> Bent needle/rod/cylinder (11%) 	11%	Rod (Bent)
<ul style="list-style-type: none"> Rod (2%) Cylinder (0.3%) 	2%	<ul style="list-style-type: none"> Straight needle/rod/cylinder (31%) 	31%	Rod
	(100%) 100%		(100%) 100%	

The objects chosen to represent these five categories as well as their determined population percentage in Earth's orbit are compiled into Table 3.4.

Table 3.4 Objects chosen for the second grab test and their dimensions.

				
Spheroid	Straight Rod	Bent Rod	Bent Plate	Flat Plate
10cm long, 7cm minor diameter 20 g	11.5in long 0.5in diameter 367 g	11 in long 0.5in diameter 376 g	7in x 5.7in x 6in 1mm thick 186 g	7in x 5.7in x 1mm 8.1cm largest diameter 186 g

4 Results

The results of the previously mentioned experiments will be thoroughly discussed in this section starting chronologically from phase one and ending with phase three.

4.1 Phase One

Phase one consisted of creating and testing the initial finger design with three different SMA wire types to determine the ideal combination.

4.1.1 Half Scale Fingers

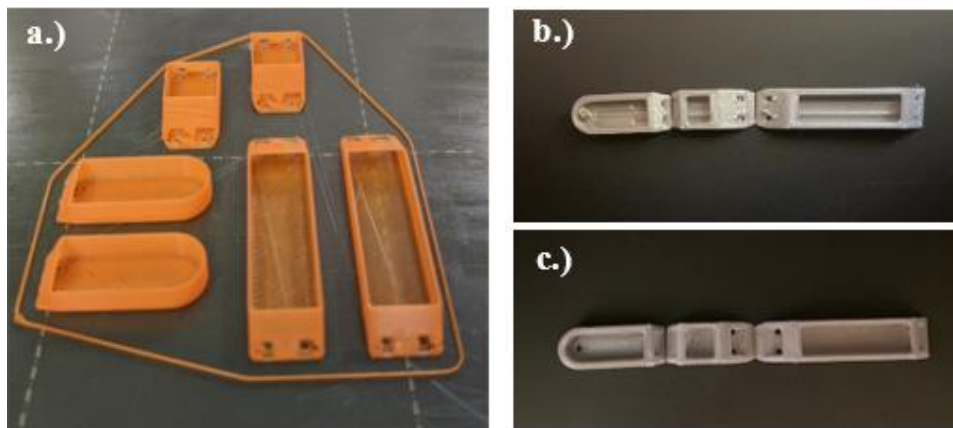


Figure 0.1. Images of each half-scale design, a) Version 1, b) Version 2, c) Version 3.

The first half-scale finger design, depicted in Figure 4.1a, consisted of entirely hollow joints with holes to run the SMA wires through, larger openings on either end for the springs to extend out of, and thin walls to keep it light weight. During the print of this iteration, many parts of this design collapsed or did not form due to the 3D printer not being capable of printing walls of small thicknesses. In the second iteration, Figure 4.1b, the walls were made to be significantly thicker, the holes for the springs and wires were adjusted to accommodate this change, and channels were created inside each joint for the SMAs to run along so they would not make contact with the springs.

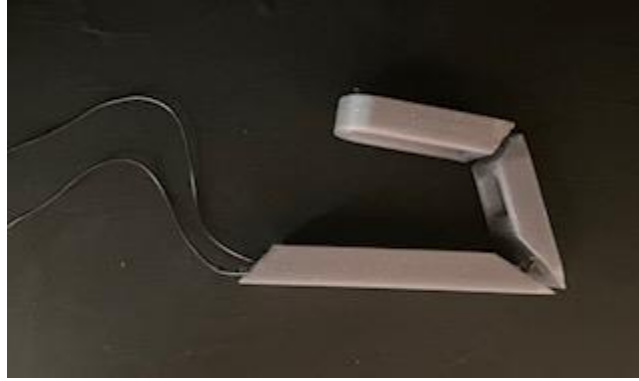


Figure 0.2 An image of iteration 2, threaded with an SMA and manually bent before testing.

Version two was printed with no issue. Once acquired, this iteration was assembled using a SMA wire with a diameter of 0.05 centimeters, transition temperature of 90°C, and length 8.5 centimeters. Upon adding the wires, it became evident that the holes meant for them did not print properly and were partially closed off internally. The wires were instead run through the openings meant for the springs as it was noticed that these openings were too small to accommodate the springs. A single fastener was used inside the final joint to keep the SMA wire in place during preliminary testing. Once assembled, the finger was manually folded until each end of a joint was flush with the following end of a joint, as shown in Figure 4.2. When connected to a power source, this iteration required 1.2 volts and 1.5 amps to fully extend. It should be noted that no hinges were attached to the joints at this time as they were meant to fit a full-size finger. This did lead to the SMAs having trouble fully extending the first and second joint despite being fully stiff throughout the rest of the finger. Additionally, the screw used to keep the wire in place in the final joint was made from an electrically conductive material and likely contributed to the amount of power being drawn. From the version two tests it was determined that the angles between the joints, 27° between joints one and two and 55° were acceptable for fully compacting Starfish into 1U but did keep it from extending efficiently

between joints one and two. It was also determined that the SMA wire would need entirely separate compartments to prevent them from making contact with any fasteners or springs as they moved during operation more than was initially expected.

For the third iteration of the finger, Figure 4.1c, fitting both the springs and SMA wire into the design was prioritized. The channels for the wire were removed to allow more internal room for the spring, and the front of each joint was made as wide as possible to fit the springs. After being printed without issue, this version was assembled. Upon assembly it was found that while the springs did fit with the wire, the springs could not fully bend the joints as they were getting caught on the upper walls at either end. These upper walls were manually removed and replaced with a few thin layers of tape so that testing could be continued. One spring of dimensions 0.3 by 3 by 10 millimeters and spring constant of 1.4 lbs/in was used in between each joint. This assembly was then attached to a power supply where it was found that the half-scale finger needed about 1.6 volts and 1.4 amps to fully extend using an SMA wire of the same specifications used in the version two tests. Both version two and version three iterations were found to extend in a minute and a half or less at the given power conditions.

4.1.2 Wire Experimentation

While shape memory wires often need to be trained via intensive heating and setting, the wires used for Starfish are only required to straighten. SMA wires are often pre-set to a fully straightened shape when sold, therefore, Starfish did not require any intensive treatment processes for its wires. Multiple spools of shape memory wire were purchased, all of which had different transition temperatures and wire gauges. This was done experimentally to determine which wire type would provide both optimal response times and the lowest power requirements. These wire experiments overlapped with the designing of the finger components done in the joint assembly tests, often being used to verify each other. As each iteration of a finger was created its

functionality was tested with the different types of wires until both the design of each joint was optimized and the best wire was determined. Initially, the joints were printed at half scale using PLA in order to make the best use of the project’s time. These half scale models were tested using three different types of wires with varying properties. The three wires chosen for this experiment along with their corresponding results of the half scale trials are listed in Table 4.1.

Table 4.1 Electrical values found during half scale trials for each wire type.

	Transition Temp: 90°C Diameter: 0.5 mm	Transition Temp: 80°C Diameter: 0.5 mm	Transition Temp: 80°C Diameter: 1 mm
Amps (A)	1.2	1.2	2.6
Voltage (V)	1.3	1.3	1.3
Time to Open Finger (s)	34	27	180
Total Power (W)	1.56	1.56	3.38

Based on the results from Table 4.1, the 1 mm diameter wire was eliminated as a potential option due to its higher power requirements and significantly longer time to fully extend a half scale finger. Once the fingers were scaled at their true size the remaining two wires were tested again. Both wires were found to resist the force of the springs at each joint and fully extend a finger with the same power requirements, about 15 watts. However, the 80°C wire was able to achieve this faster than the 90°C wire. Therefore the 80°C wire was chosen for the full mechanical assembly tests.

4.2 Phase Two



Figure 0.3 The preliminary full-scale design.

After these preliminary tests were completed, all aspects of the design that needed to be adjusted or changed were used to create a preliminary full-scale design. As shown in Figure 4.3, special channels were created for the SMA wire to be run through so that it could avoid all contact with any fasteners and springs as well as maintain its “U” shape in the final joint. Adequate space was given for the springs and their mounting fasteners. The width of the full-scale version was sized up an additional 0.25 centimeters so that the wire could be bent into two “U” shapes instead of one, thus quadrupling the expected amount of force produced by the wires. This preliminary version was assembled to briefly verify the design's functionality. The wire and springs fit with no issue inside the full-scale design, though it was noted that an additional guide loop would be needed in the third joint to keep the wire in that portion from moving during use. The springs were also scaled up for this design, two springs with dimensions of 0.4x4x10 millimeters and a spring constant of 4.14 lbs/in were used between joints three and two. Two springs with dimensions of 0.4x4x15 millimeters and a spring constant of 1.4 lbs/in were used between joints one and two. This assembly was subjected to a power source at 2 volts and 1.5 amps. During this test, the wires could be seen straightening, but the assembly only twitched and did not straighten as it had for the half scale version at these power inputs. The power was then gradually increased but still had no effect on the assembly despite the wires being fully

straightened in some places. At this point the wires reached well above the melting temperature for PLA and the assembly began to structurally fail in some places due to the heat. Power was turned off and the assembly was left to cool down. It is believed that the reason it did not straighten was due to the increased stiffness of the springs. This would explain why the wire appeared to be fully straight in some places but not at the end of each joint where the springs were located, the wires were not strong enough to resist the force of the stiffer springs. While the geometrical specifications of the springs were adequate, springs with a lower stiffness were needed to allow the joints to fully extend.

4.3 Phase Three

4.3.1 First Full Assembly



Figure 0.4 Images of Starfish moving from its compact to fully extended phase.

The final full-scale design for Starfish, shown in Figure 4.4, is built upon all lessons learned from previous iterations, with the addition of built in hinges at the end of each joint. Inside each joint, special channels and walls were made in order to keep the SMA wire from interacting with any other components during its operation. Each full finger bends the wire into two separate “U” shapes, a common technique in soft robotics used for multiplying the force output of a single

SMA wire. Coverings for each of the joints were created so that grip force could be measured without the risk of electrocution. The hollow base plate has a maximum of five fingers mounted to it and acts as housing for Starfishes camera and LED lights. To fit the entirety of the design into 1U, the back edges of each joint were given fillets of 0.2-0.3 centimeters. It was determined that Starfish should keep all essential electronics, such as its control board and power supply, in a separate bus in order to protect the essential components from debris.

It is acknowledged that insulation should be placed internally and externally over Starfish as a means to protect the SMA wires from the potentially harmful effects of a space environment as well as keep them from activating should they be exposed to higher environmental temperatures. However, the inclusion of this insulation membrane is not within the scope of this thesis and will not be included in testing as the design and operation of the Starfish mechanical system is most critical.

4.3.2 Mechanical Assembly

To assemble the first version of Starfish, roughly 4.5ft of 80°C shape memory wire was used. This wire was threaded through the base and through each individual finger. To begin, finger pieces were individually threaded onto the wire. Once one finger had all joint pieces fully threaded, the springs and lids were attached. It should be noted that much like actual tendons, the shape memory wires needed to have extra length in each finger so that they could fully extend. This was realized after the first attempt of the assembly when the fingers were not able to fully extend and therefore caused minor damage to pieces of the fingers via melting. This extra wire in places would best be accommodated by adjusting the shape of the lids to allow for this extra length to be stored properly. Once a finger was added to the wire as well as the main base plate, it was manually tested to see if it could fully extend. If successful, the next finger would be added via the same process. If unsuccessful, the finger would be re-threaded to allow for the

correct amount of wire length to allow for it to extend. Once all fingers were threaded and fully assembled, the back of the main base plate was added, and the final springs attached to the fingers. Figure 4.5 shows the fully assembled Starfish made from PETG.

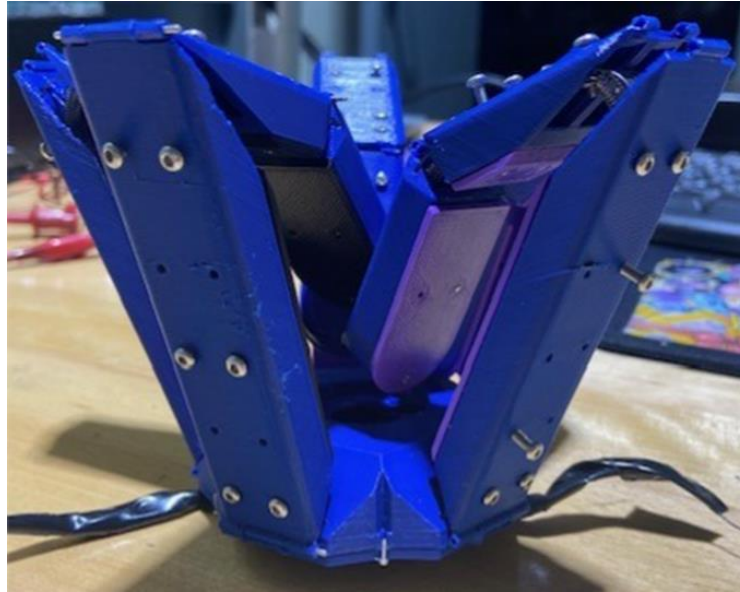


Figure 0.5 Fully assembled PETG Starfish.

It can be noticed in the right most visible joint in Figure 4.5 that the joint is not attached properly and that some of the joints do not fully close. This is because the extra wire length is keeping those joints from doing so. Regardless of this unforeseen issue, this iteration of Starfish was still able to be tested. When power was applied to Starfish, its fingers began to open one at a time as the wire heated up. However, after some of the fingers opened a small amount, the first three fingers in the series stopped extending. This was a result of the wire becoming too hot within them and melting through portions of the finger shells, causing the wire to get stuck and not be able to extend further.

4.3.3 First Grip Test

The chosen objects were lowered into Starfishes grip using the testing machine and by manually opening Starfish so that the object could be placed within its grasp. Due to the damage

already sustained in places from the first assembly test, it was deemed not worth the risk to have Starfish turned on to fully extend and then grasp the objects itself at this time. While this may seem concerning it must be remembered that the grip system of Starfish was designed to be entirely passive. This means that it needs no power whatsoever to close around and maintain its hold on an object, only to open it. Therefore, manually holding open Starfish and allowing it to close itself around the objects should produce the same results as it would if it were allowed to fully extend itself using its own power. That being said, 10 to 11 tests were performed on each of the five objects described in Table 3.2 and the following force-extension plots were generated using every third data point from the full data set to depict the average from each object's respective tests. This was done because 100 data points did not neatly convey the data on the plot space. An additional force-extension plot depicting the full results of one test for the corresponding object has been included as they allow for certain physical results to be seen. It should be noted that due to the orientation of the load cell, the positive direction is downwards, and the negative direction is upwards.

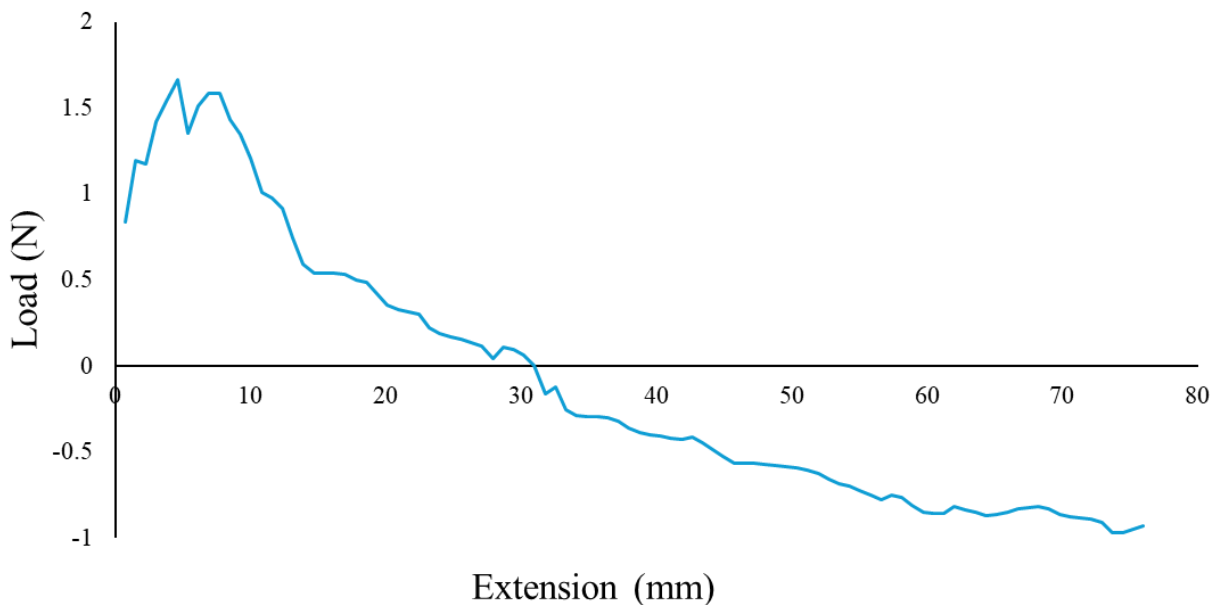


Figure 0.6 One load versus time tests for the rubber ball.

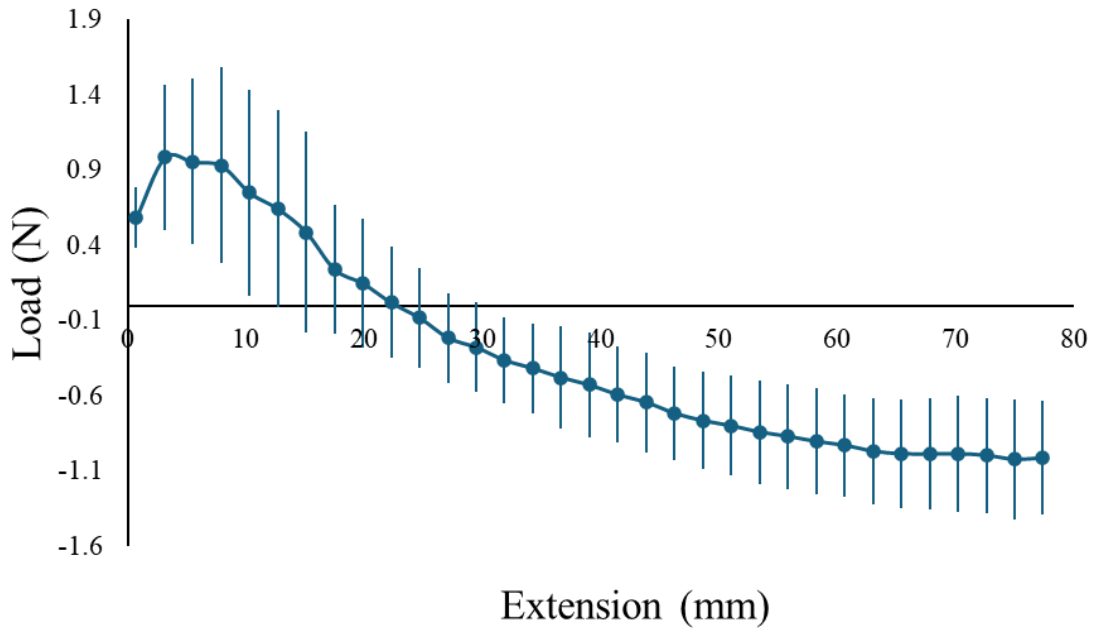


Figure 0.7 The average of all ten rubber ball tests with standard deviation.

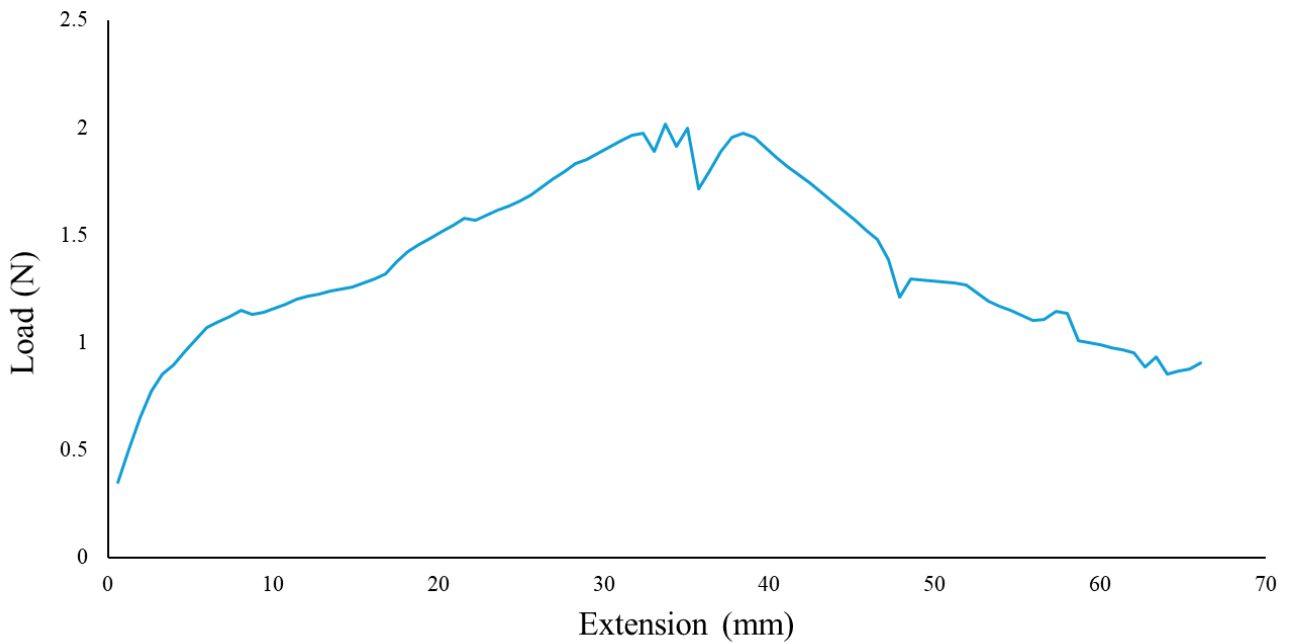


Figure 0.8 One load versus time tests for the bike pump.

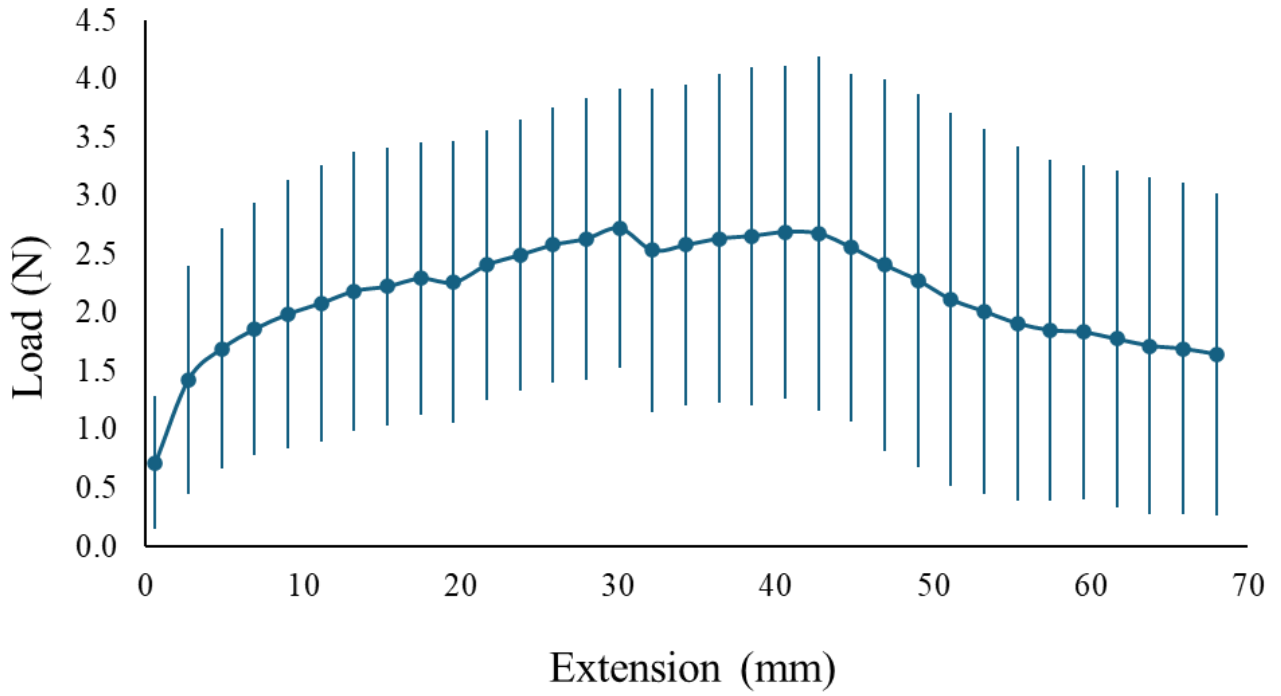


Figure 0.9 The average of all ten bike pump tests with standard deviation.

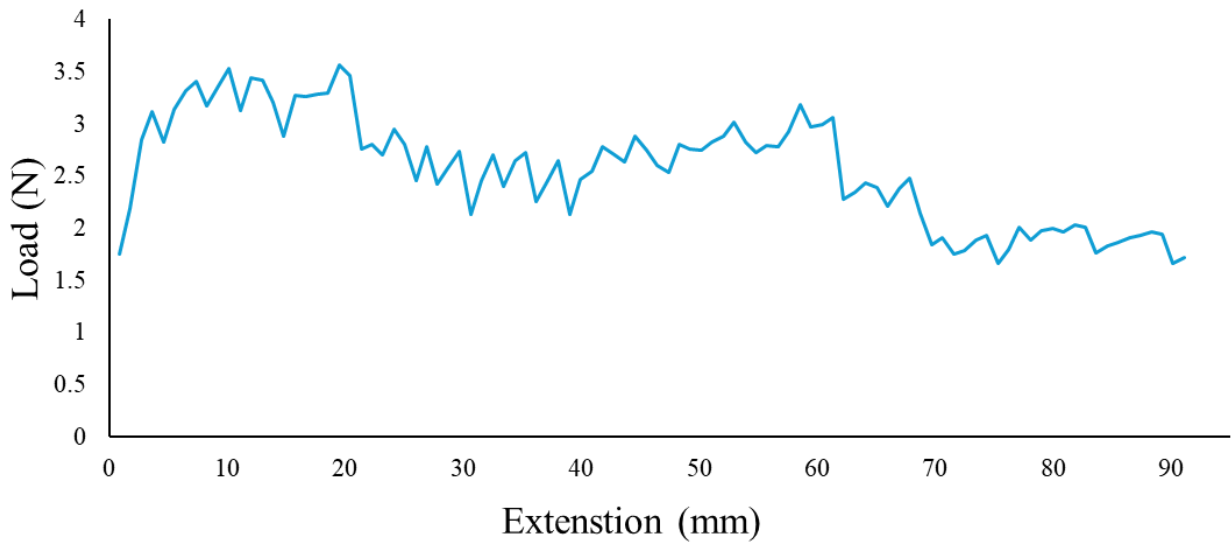


Figure 0.10 One load versus time tests for the craft cube.

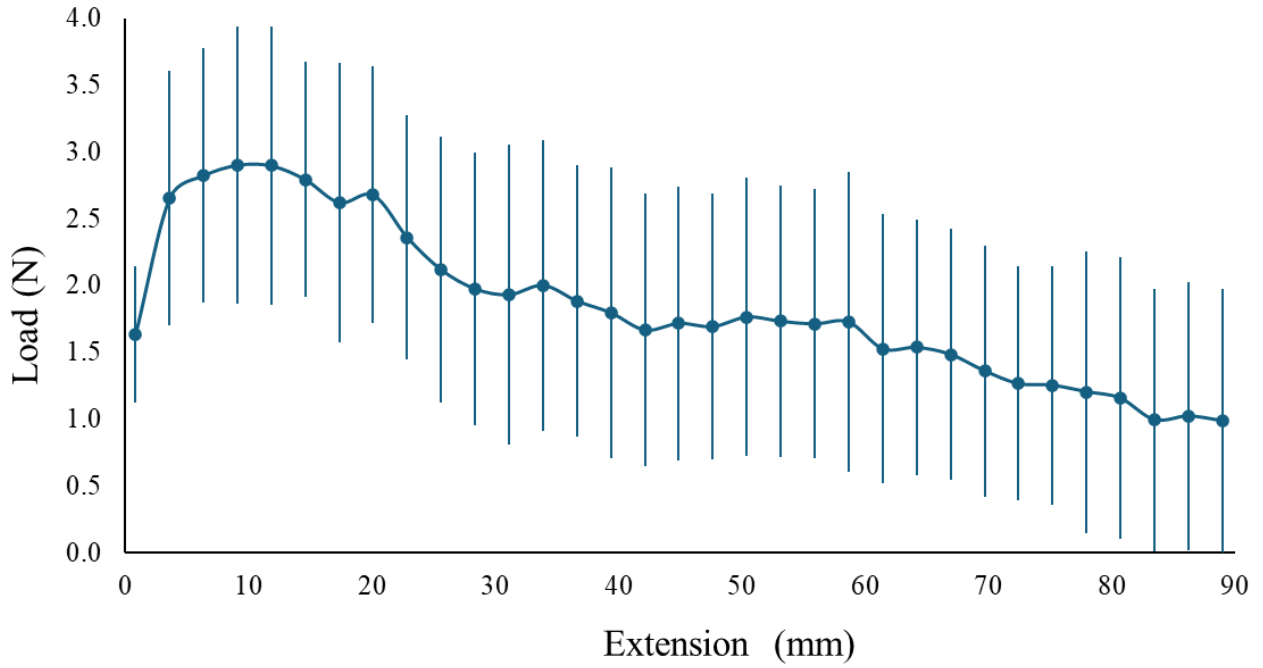


Figure 0.11 The average of all ten craft cube tests with standard deviation.

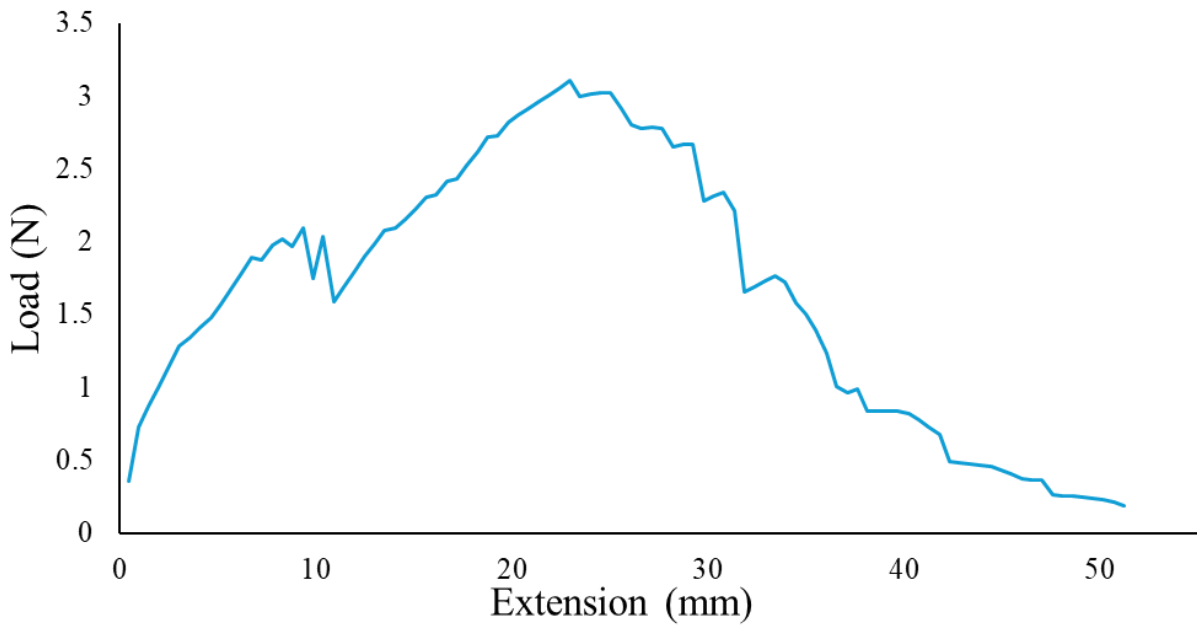


Figure 0.12 One load versus time tests for the glass.

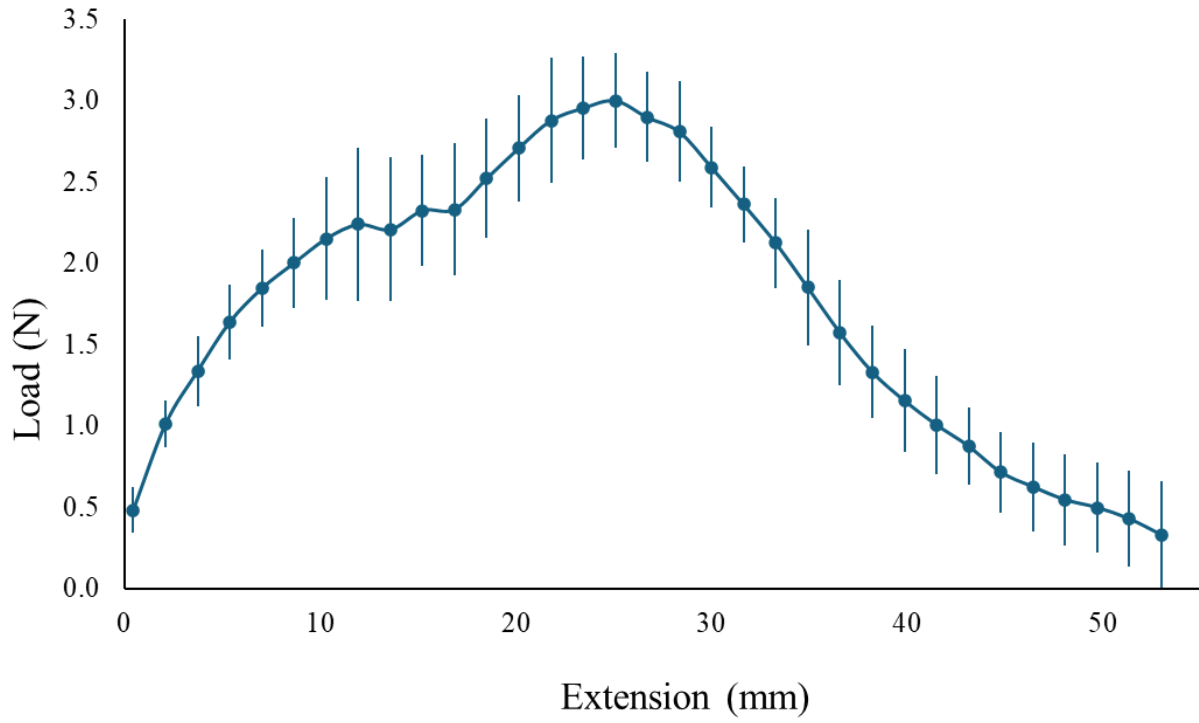


Figure 0.13 The average of all ten glass tests with standard deviation.

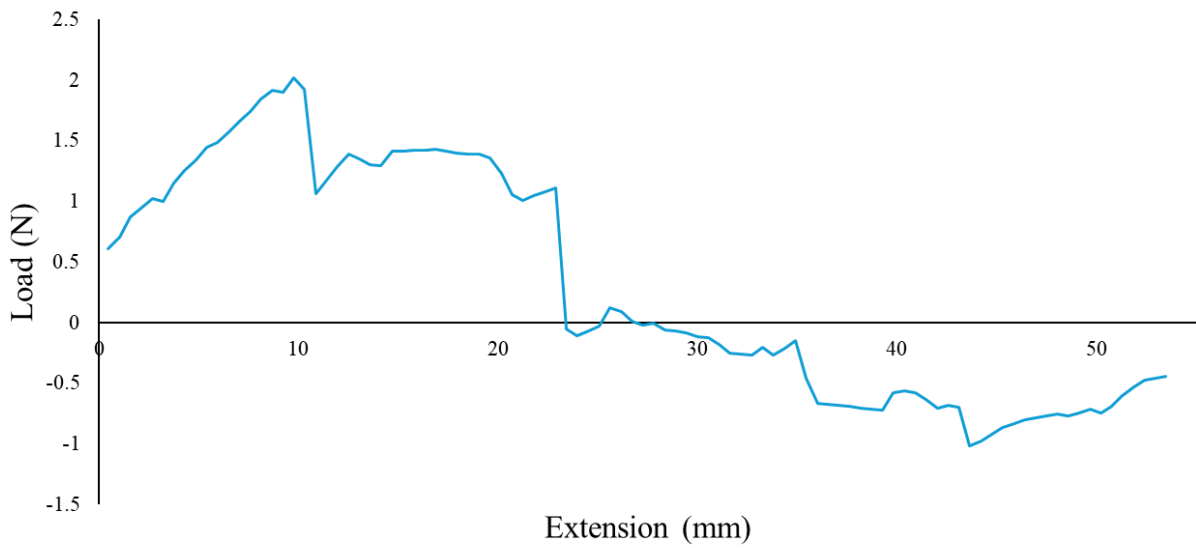


Figure 0.14 One load versus time tests for the metal cone.

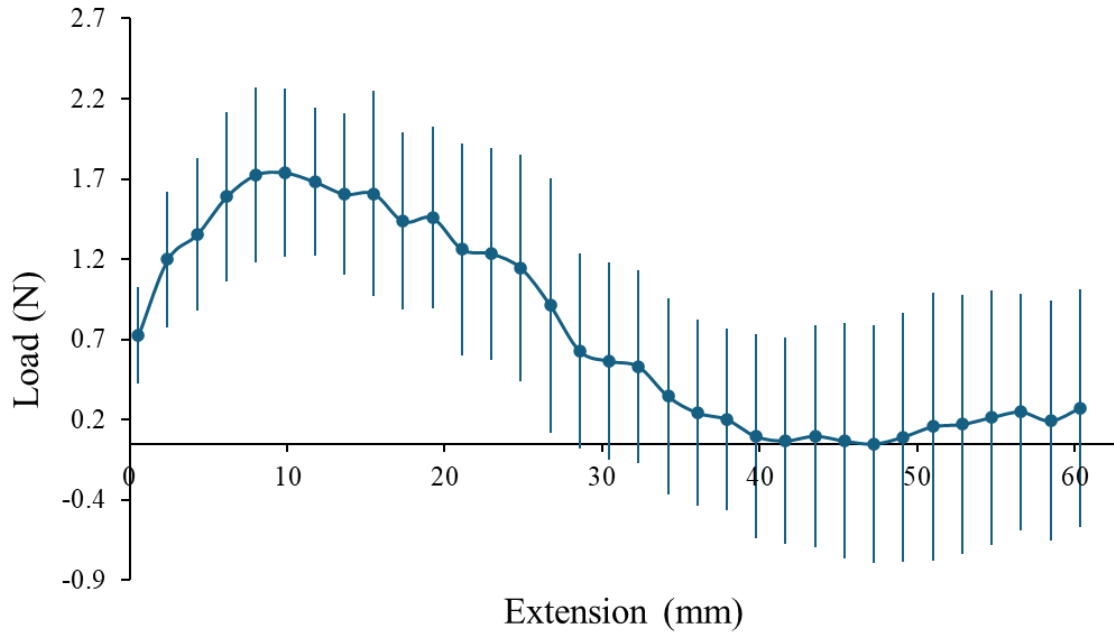


Figure 0.15 The average of all ten metal cone tests with standard deviation.

4.3.4 Issues with First Assembly

The most critical issue with the first assembly was the effects the amount of heat produced by the wires had on the finger structures. Despite being made of PETG, the heat from the wires caused the material to warp in places where it was thinnest. These places being the guide holes on either end of the bodies and the walls used to separate the wires from each other. This warping caused some wires to become stuck inside the material after the power was disconnected. When being freed from the material, some of the wires snapped due to how embedded in the material they were, requiring that the whole length of wire in the first assembly be replaced. The wires were not insulated in this first design as it was believed the PETG could withstand the heat due to its high melting point. However, prolonged exposure to the lower heat from the wires caused the material to soften and deform. This deformation also affected adjacent

finger components by melting the joints between each component together, preventing the fingers from being able to extend.

Additionally, the continuous SMA wire woven throughout all five fingers contributed to issues as well. The fingers wired closest to the beginning of the circuit heated much faster than the fingers at the end of the circuit. This means that while the end fingers were still nearing the transition temperature the beginning wires were exposed to it for significantly longer, resulting in the most catastrophic material failure to occur in them. This wire layout also caused the fingers to open at different times rather than all at once, while not a major issue this could still result in issues with capture down the line. An unexpected consequence of this wire layout was the length of wire present inside the finger bodies. When not in use, the wire bunched up inside the body; when heated again, this bunched up wire would heat into and become trapped in the body coverings, preventing them from extending and thus preventing the finger from extending as well. To prevent this in future designs, a method to house the internal wire properly would be needed.

4.4 Second Full Scale Design and Testing

The second full scale design focused on correcting issues present in the previous design. A return to literature was made to guide this process and analyze how others had solved these issues.

4.4.1 Design Changes

Firstly, the wires were separated into one wire per finger rather than one large wire. As connecting shape memory wires is notoriously tricky due to their shape changing properties and small diameters, small rhodium jewelry crimps had to be used on either ends of the five wires. These crimps were then connected to each neighboring shape memory wire in series by soldering normal wire of the same wire gauge to them. This eliminated the issue of the SMA wires located

in the palm housing from connecting when they moved and shorting the circuit. Additionally, due to the structural failure from the heat, portions of the 80°C wire were unable to be recovered as it had become trapped within the melted PETG. Therefore, the 90°C wire had to be used in its place.

Secondly, the wires were previously uninsulated due both to perceived ability of the PETG to be able to handle the high temperatures that the wires emit and due to the difficulties in acquiring insulation in the size appropriate for the wires. The results from the first full design show that the insulation of these wires is absolutely crucial for Starfish to operate nominally. To solve this issue, each of the five wires were insulated by hand using small segments of heat shrink. This did not fully eliminate the heat issue but did allow for the next iteration of Starfish to become operable multiple times in a row without failing.

Next, the layout of the wires themselves were revisited after additional research into shape memory alloys used in specifically hand prosthetics was conducted. It was seen that many prosthetics utilizing SMAs require a great deal of power and complexity to operate fully and also occasionally need additional shape memory wires at the joints to help them fully open.

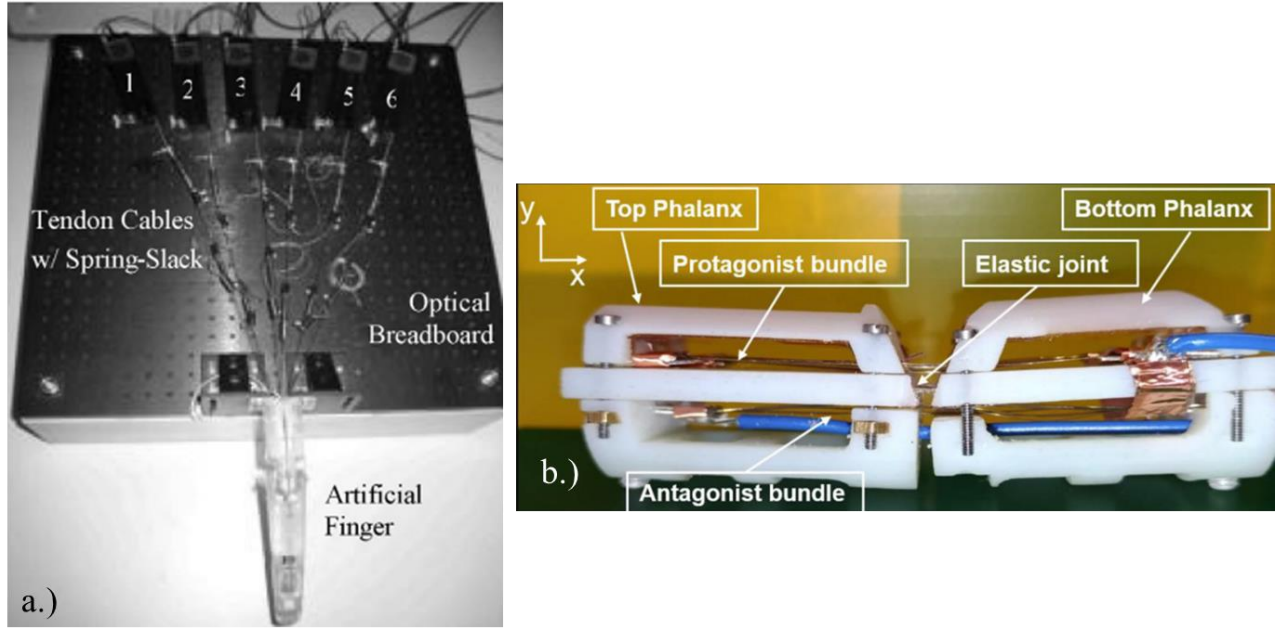


Figure 0.16 Examples of two more complex SMA finger designs for prosthetics [53], [54].

Figure 4.16 shows two separate designs for a biomimetic finger prosthetic actuated by SMA wires. In 4.16a, the finger is actuated using individual six individual cables, attached at either end of the artificial finger. In 4.16b, multiple bundles of SMAs are used on the top and bottom with additional wires located in between the finger joint as bending support. Using these designs as influences, two new wire layouts for the fingers were created and tested.

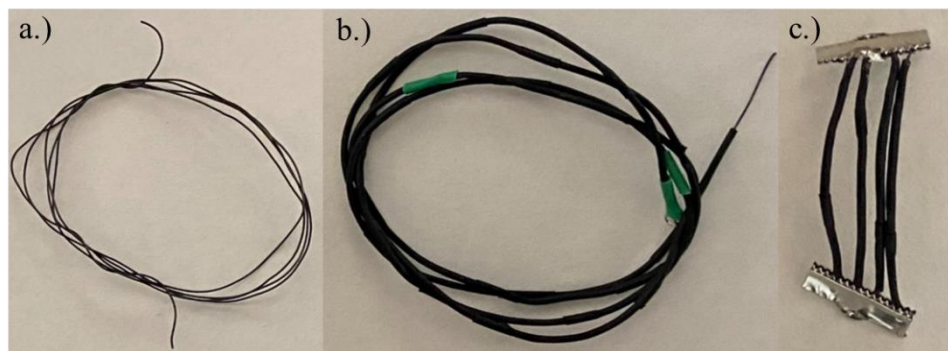


Figure 0.17 Depicts the three different types of wire configurations used for the finger designs.

Figure 4.17 shows the original wire used for Starfish in 4.17a as well as the two new wire configurations in 4.17b and 4.17c. The design in 4.17b is a shorter length of wire that is insulated

along its length using heat shrink and crimped at one end using a rhodium jewelry crimp. Five of these insulated wires attached in series would be used in place of the long continuous length of wire used in the original design. The design in 4.17c operates similar to the supporting joint wires seen in figure 4.16b. Here, two long nickel fabric clamps were used to hold four short lengths of insulated wire in place to act as more of a muscle than a tendon.



Figure 0.18 Image of new finger design.

In Figure 4.17 a, the original finger design relied primarily on using the shape memory wires to push the joints apart while also being free to move within the finger shells. The designs in Figure 4.17b and 4.17c however, use the SMAs to pull the joints apart from fixed positions much more similar to the extensor tendons in the human hand would. Both of these new designs benefit from using less wire than the previous design which results in less power consumption overall. The design in 4.17b uses 32 inches of 90°C shape memory wire that is threaded through the actual finger shells. This was done to eliminate the extra free moving wire within the shells causing damage to the outside where they can help the joints move more freely. This threading of the wires is also done in a similar U-shape fashion as in the first design. This keeps the increase in actuation force while also allowing the wires to “pinch” the backs of the finger shells, resulting in better control in the movement of the joints during actuation.

In 4.17c, the design utilizes four short 7cm lengths of shape memory alloys joined in parallel, secured together by using a longer toothed jewelry clamp. This design functions more as a muscle than a tendon as it is a small cluster of SMAs used at the edges of the joints for actuation. This design posed many challenges during its fabrication as the smaller wires often broke loose

of the clamp during actuation despite the clamp being soldered shut. Moreover, this design required at least four amps to operate and caused the metal clamps to get hot, raising concern of whether it would melt through the PETG. Ultimately it was decided that the design in image b was best suited for implementation.

Another design change that was made was the strength of the springs at each joint. In the original design, two springs with a rate of 1.4lbs/in were used per joint. While this posed no issue to the wires ability to open joints one and three, joint two consistently struggled to open. While the new wiring design did help in opening this joint further, it still wasn't enough to make it fully extend. Two new sets of springs of rates 1.1 lbs/in and 0.95 lbs/in were acquired and tested at this joint.

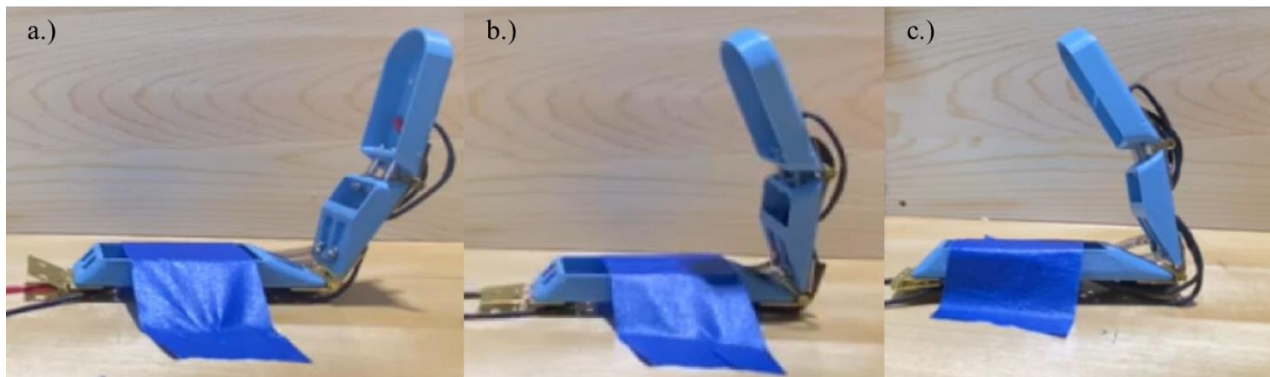


Figure 0.19 Images of fingers at max extension using a) 0.95 lbs/in, b) 1.1 lbs/in, and c) 1.4 lbs/in springs.

The max extension during actuation of each of these three springs is shown in Figure 4.19. As can be seen the 0.95 lbs/in springs allow the finger to extend the farthest, though notably still not far enough to achieve full extension. It is possible that the fingers would extend farther than what is shown in the figure if left to sit for a longer duration of time, but this does risk the material failure of the finger shells. Therefore, all springs at the second joints were replaced with the 0.95lbs/in springs and the 1.4 lbs/in springs were kept at all third joints since they were still able to fully extend there.

As for the first joint, and the last design change made between the first and second assemblies, the springs were switched out according to the order that they receive power. In the original design, the fingers would open one at a time starting from one end of the wire to the other. This would cause the first finger to be subjected to the joule heating for a longer duration than the final finger and would cause it to actuate the fastest as well as structurally fail first. While the heating cannot be mitigated, to control the rate at which the fingers open and have them open at the same time, different strengths of springs were used corresponding to a fingers order in the circuit. The first and second fingers were given the strongest springs of 1.4/lbs/in, the third and fourth fingers were given the 1.1lbs/in springs, and the fifth finger was given the weakest of the springs, 0.95 lbs/in. This caused the first two fingers who receive power the fastest and for the longest duration to open slower while also letting the fingers that are weaker due to having to take longer to heat up open faster with the weaker springs. During operation, this results in a nearly synchronous actuation between all of the fingers. The second full iteration can be seen in Figure 4.20.



Figure 0.20 Image of the full second iteration of Starfish.

4.4.2 Second Assembly Testing Results

The resulting force versus time plots for the second assembly test are shown in the figures below.

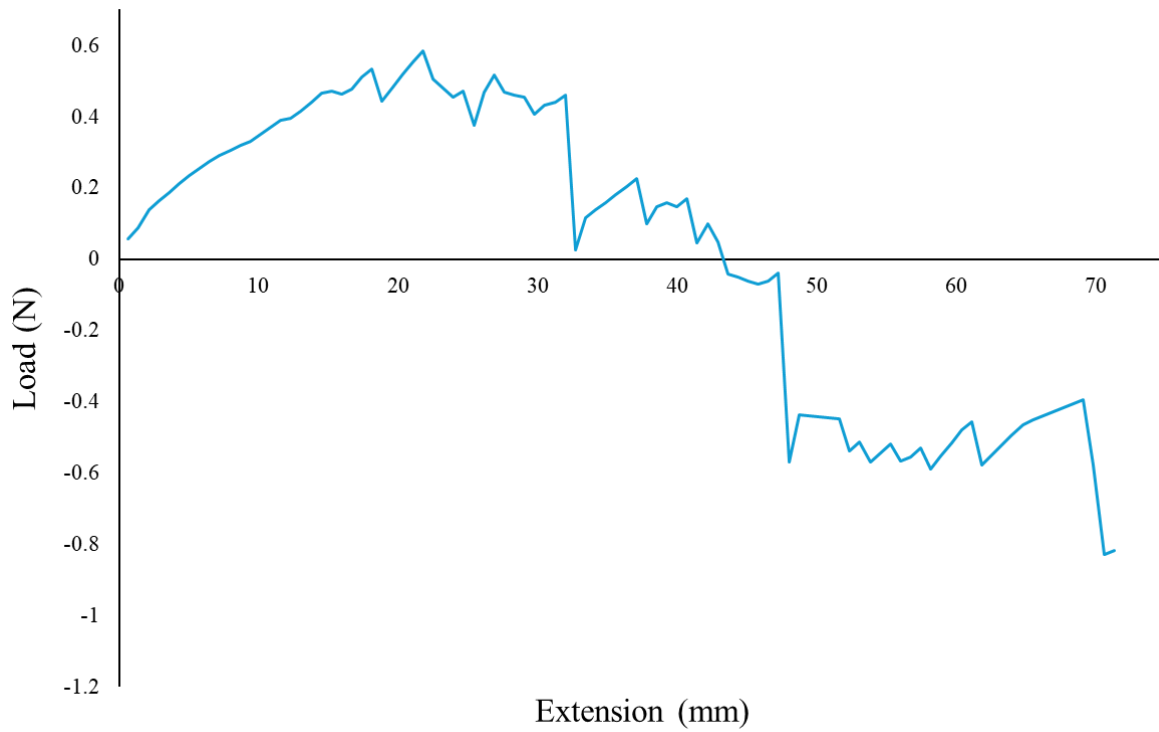


Figure 0.21 A single load versus time test for the spheroid object.

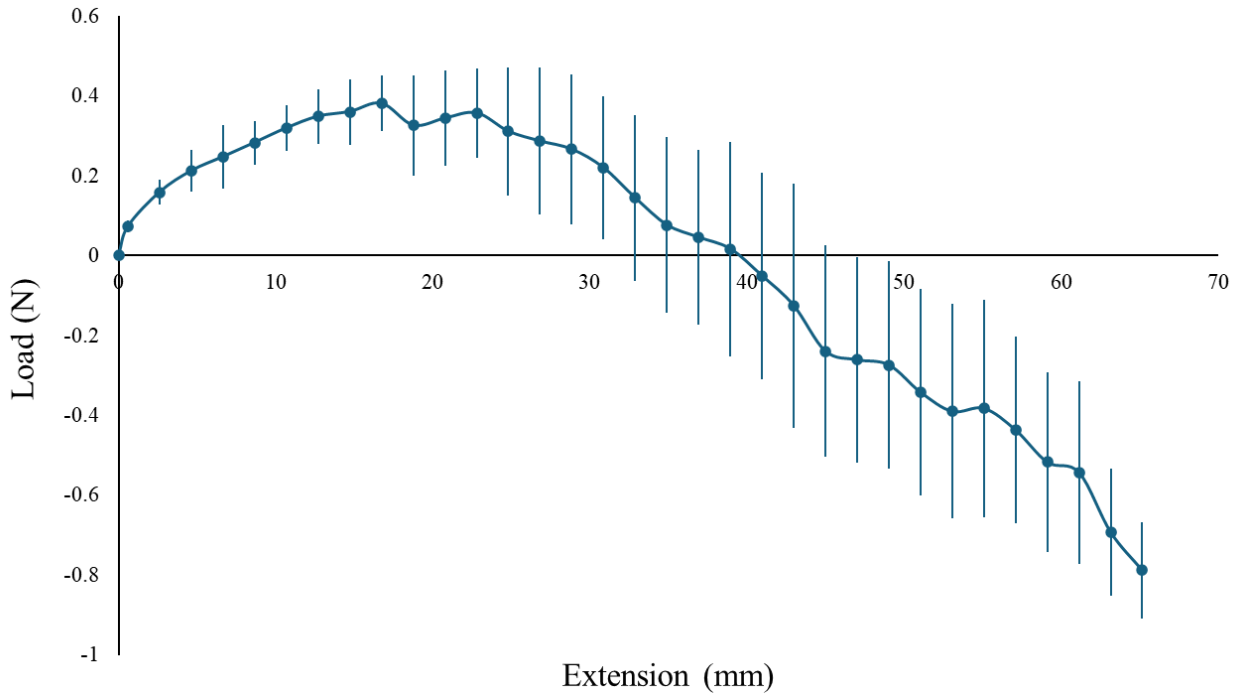


Figure 0.22 The average of all ten spheroid tests with standard deviation.

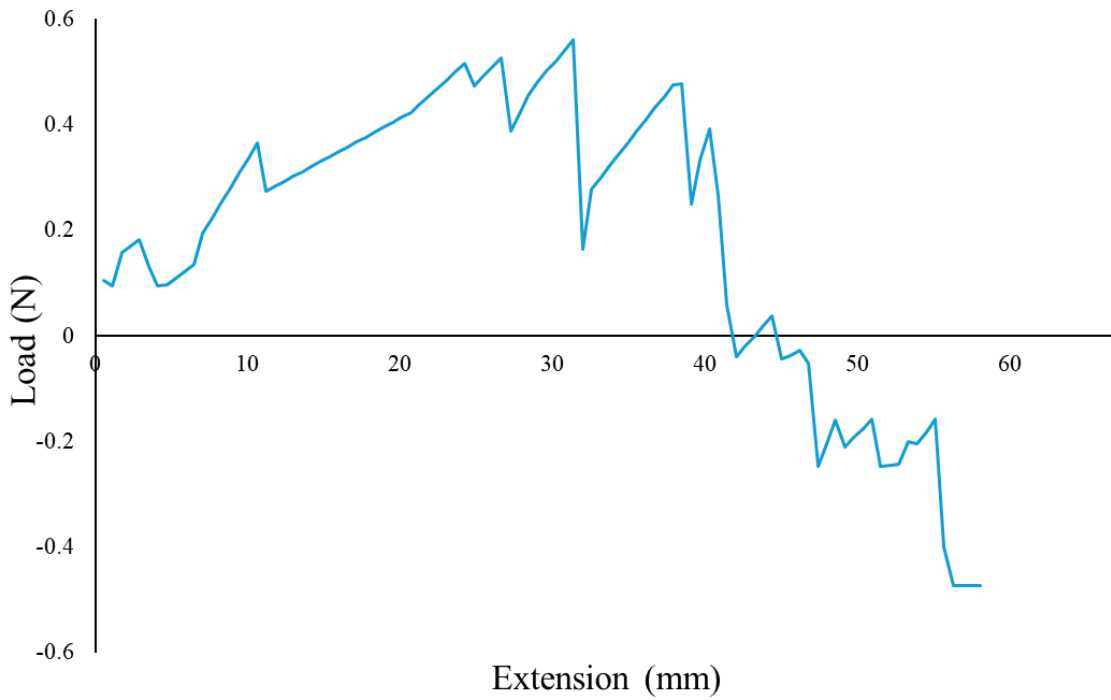


Figure 0.23 One load versus time tests for the straight rod.

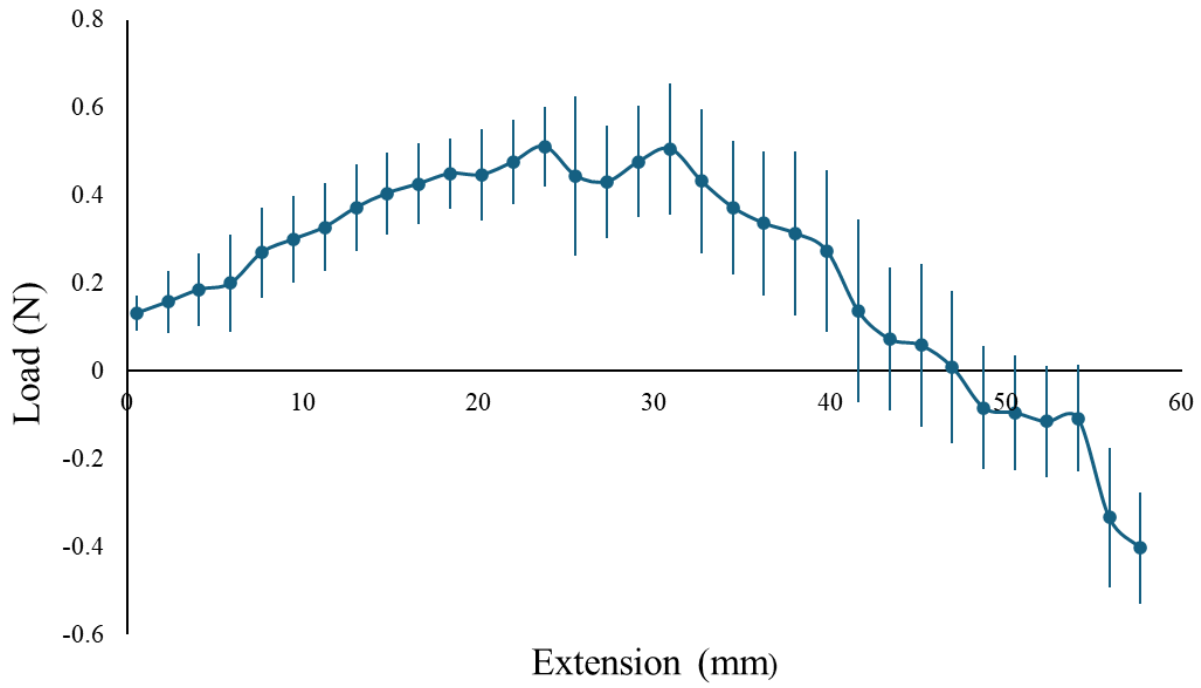


Figure 0.24 The average of all ten straight rod tests with standard deviation.

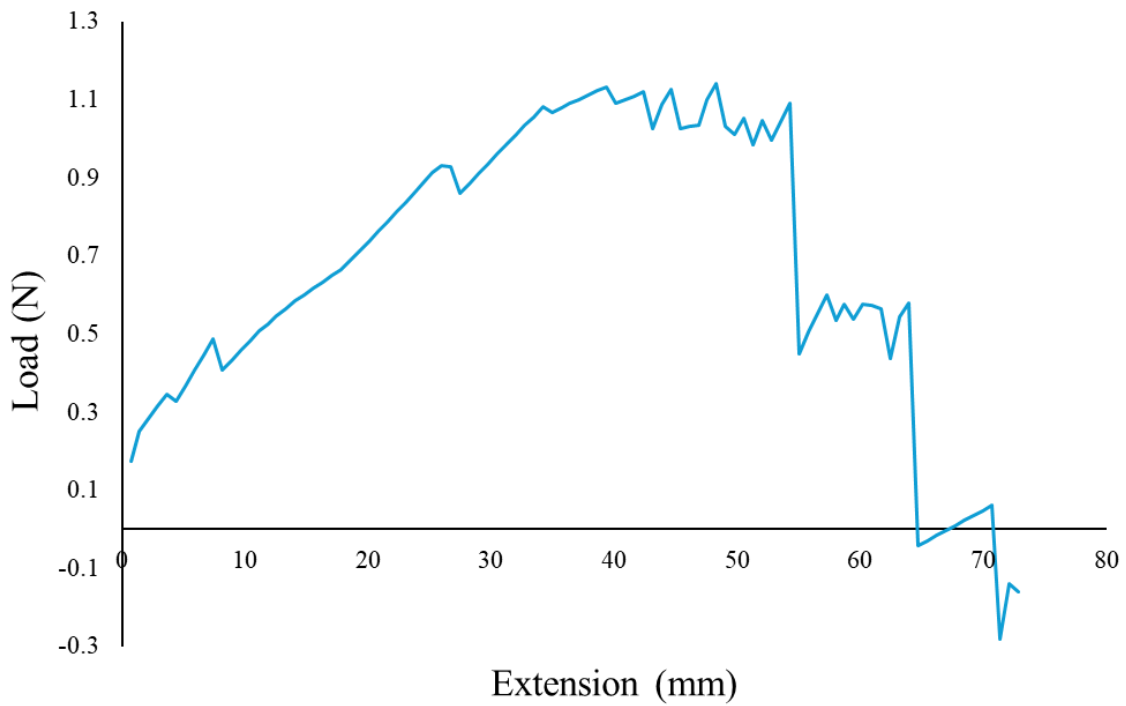


Figure 0.25 One load versus time tests for the bent rod.

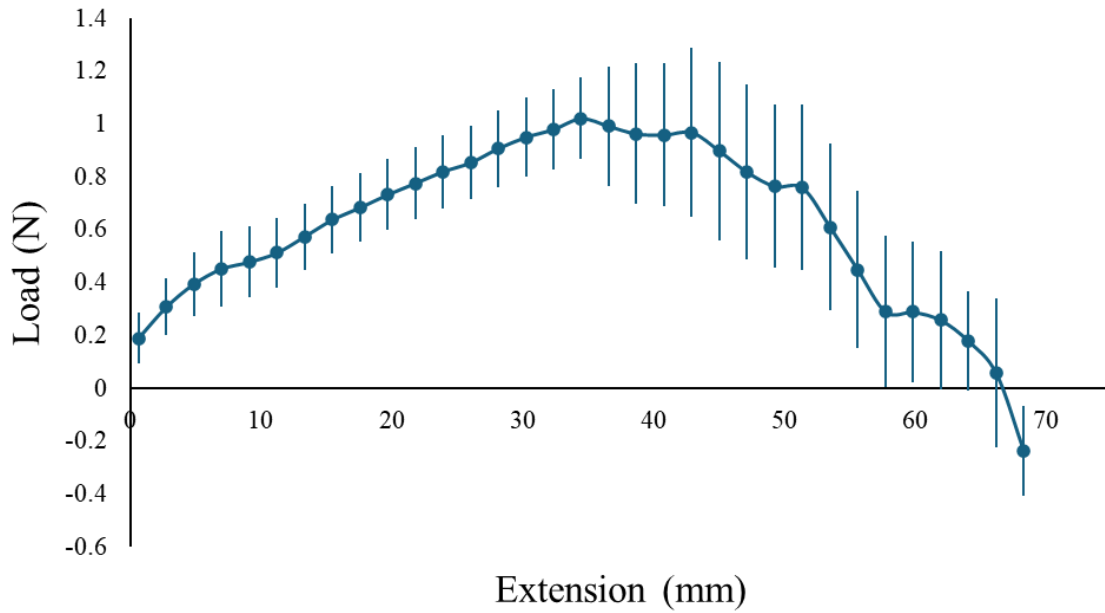


Figure 0.26 The average of all ten bent rod tests with standard deviation.

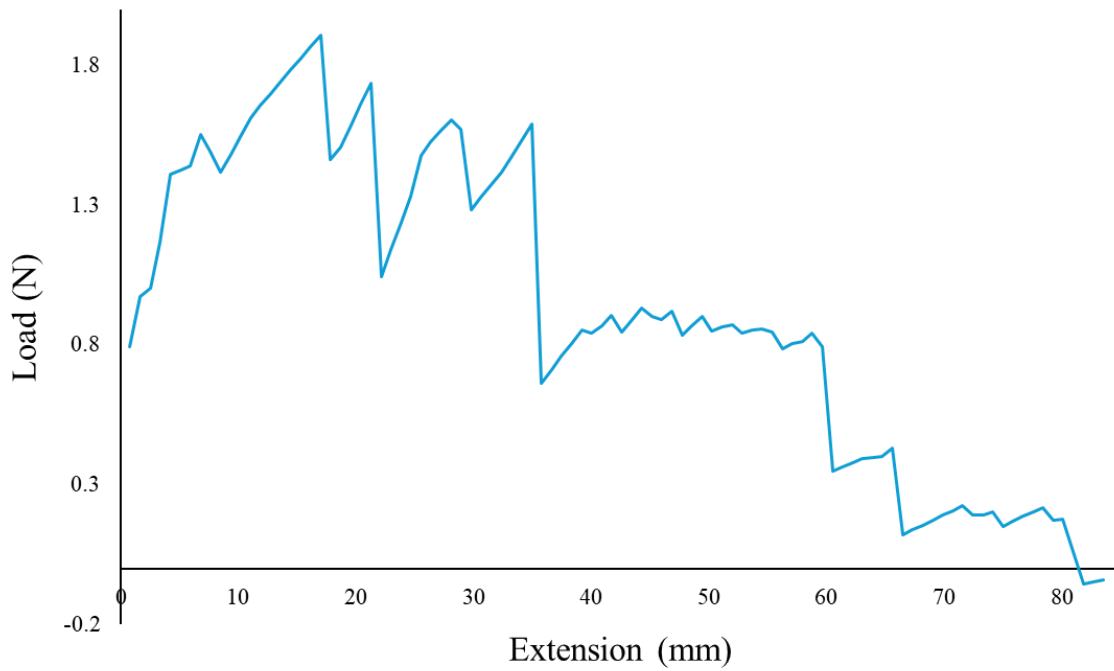


Figure 0.27 One load versus time tests for the bent plate.

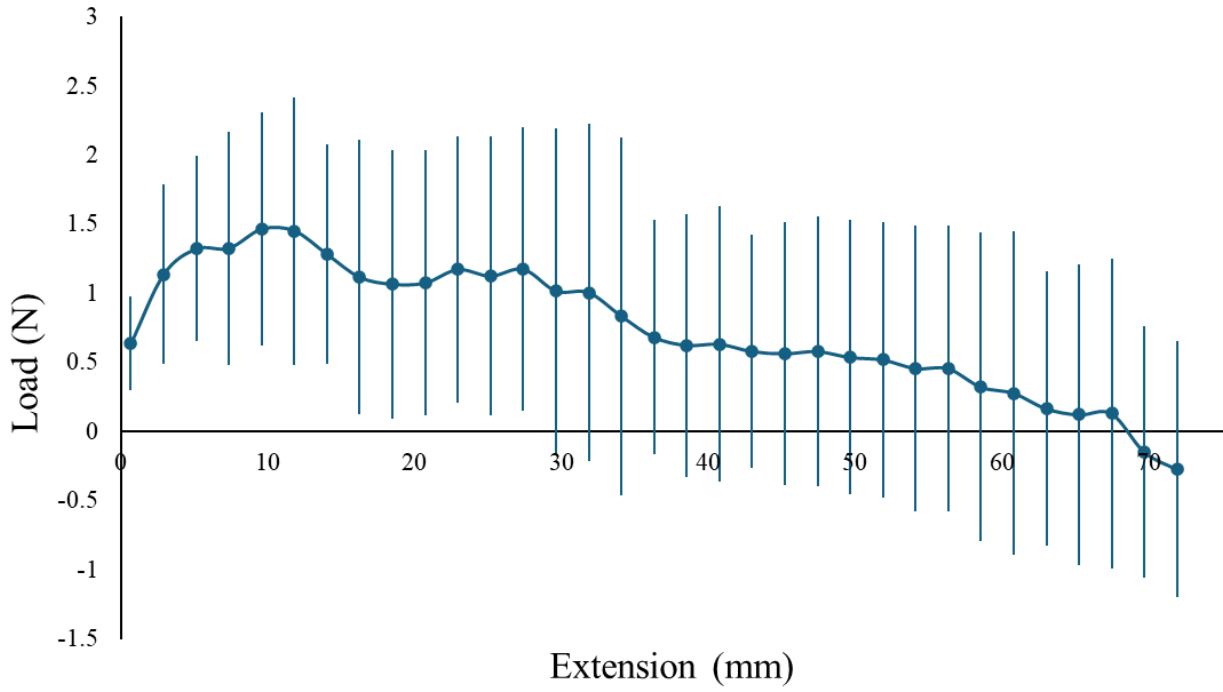


Figure 0.28 The average of all ten bent plate tests with standard deviation.

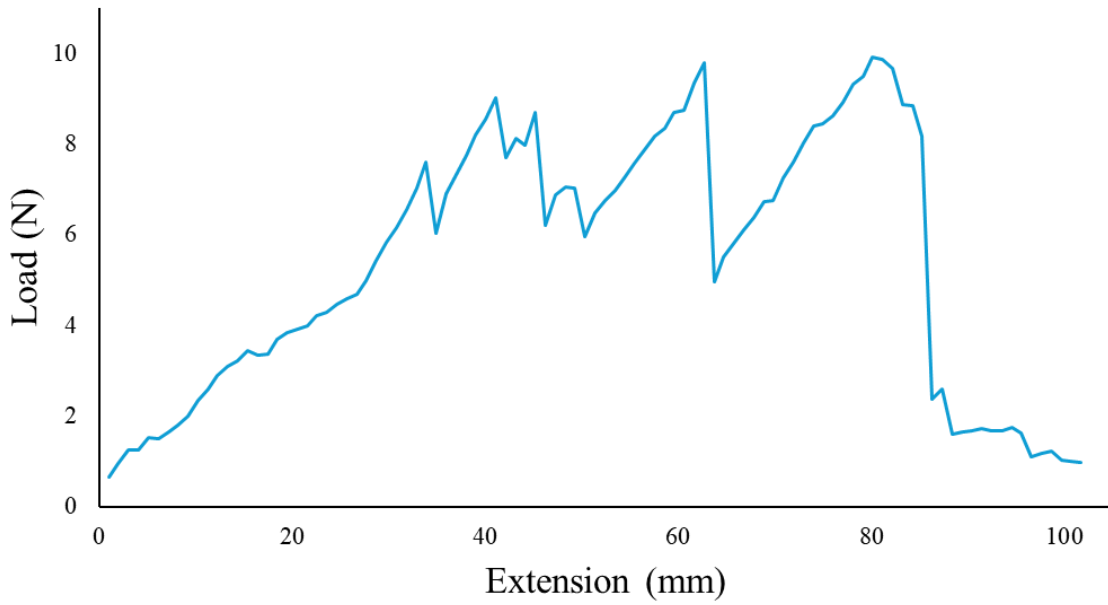


Figure 0.29 One load versus time tests for the flat plate.

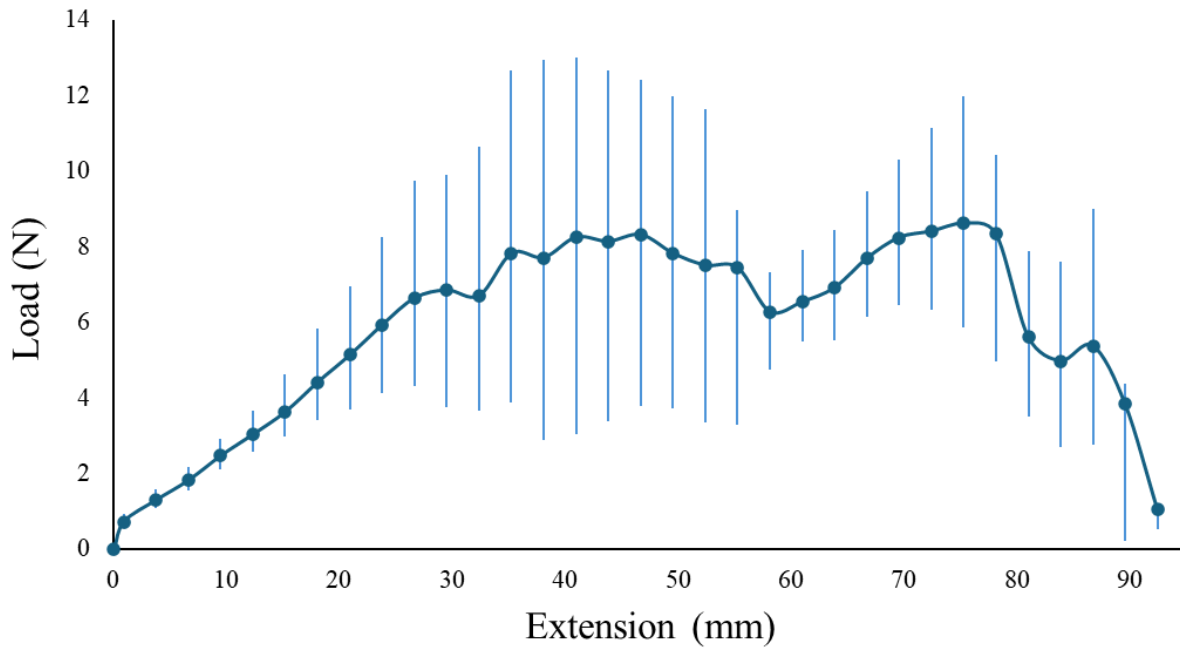


Figure 0.30 The average of all ten flat plate tests with standard deviation.

5 Discussions, Conclusions, and Recommendations

Further discussion on the results from all tests will be discussed in this section. Starfish's abilities will be compared to current proposed ADR methods in order to determine how it performs against them. Final recommendations on how to improve the Starfish design will also be discussed.

5.1 Discussion

5.1.1 First Grip Test Discussion

A majority of the single test plots show a similar initial trend wherein the highest pull forces produced are experienced at the very beginning of each test, indicating that Starfish produces a consistently firm grip when it first captures an object. All three of the more cylindrical objects had varying lengths, which demonstrates that Starfish is not bound by an object's dimensions parallel to its base, only perpendicular, as demonstrated by the craft cube and rubber ball. This is very similar to how an actual human hand might struggle with grasping certain objects. For example, a pencil is as easy as a broom to maintain a grip on with one hand despite their vast differences in size and weight as opposed to a beach ball. This is because the size of the beach ball exceeds the diameter of an entire hand and therefore does not allow the fingers of the hand to bend enough around the object to maintain a firm grip and requires little force to be pulled away.

It was anticipated that, due to the extension springs between each joint, the fingers would close tighter around a captured object should it move within or out of Starfish's grasp. This behavior can be somewhat seen in the single test figures but most clearly in Figures 4.12 and 4.14 by the increases in force after sharp drops occur. These drops indicate where a single finger releases from the object. The steady ramp back up in force is due to the rest of the fingers closing more securely around the object due to the space made from the single finger detaching and from

the movement of the object allowing more space to contract. This ability acts as a passive readjustment of Starfish's grip; it also allows Starfish to be adaptable to objects of all shapes and sizes. Figure 4.12 demonstrates Starfish's ability to maintain a firm, but not crushing, grip on fragile objects. Had this glass vase been subjected to a strong crushing force it would have shattered. However, no damage of any kind was observed during any of its tests. This ability to grab fragile objects would allow Starfish to capture materially degraded or potentially volatile debris with a low chance of shattering it and thus preventing more debris from being formed.

The final power requirement for this iteration of Starfish was around 42 watts assuming no additional electronics such as the camera. It should be noted that while at this power requirement, Starfish's fingers do extend, they were incapable of completing the full 180° extension due to the angle size between the first and second joint and material limitations. This occurred because the wires needed time to stiffen enough to push apart these two joints since they have the farthest distance needed to fully extend. During this extension time however, the SMA wires heat up past a sustainable temperature for the PETG. The wires then begin to move through the PETG instead of extending between the joint, preventing it from fully opening and causing moderate to severe damage to the PETG part. This can be easily prevented in the future by using a metal material with insulation for Starfishes structural components as opposed to PETG so that it won't be affected by the heat produced by the wires.

5.1.2 Second Grip Test Discussion

The second full Starfish assembly required much less power to operate, typically 36-40 watts. Also, this iteration could open and close roughly 45 times before any changes in actuation or material were noticed. Minimal material deformation occurred at the second body segments of the fingers as well as in the guide holes at the base plate after these actuation cycles. The fingers were able to extend, though not fully, due to the insulation within the base plate melting together,

preventing the wires from stretching their full length. The amount opened did still allow the test objects to be pushed through Starfish's fingers and their ability to grab the object to still be tested.

Figure 4.21 shows one load versus extension tests out of the ten performed on the spheroid object. When compared to the ball from the first test, it can be seen that both plots follow a similar trend. That being that Starfish's is able to capture the objects but as the objects move out of its grasp, rather than the fingers tightening around the object as its pulled from its grasp, the spherical objects are instead pushed further out of Starfish's grasp as is evident by the negative readings. The results of Figure 4.21 do show however that Starfish could hold onto the spheroidal object a little bit longer than the ball, though with much less of a grip force being applied, an average max force of 0.4N compared to the balls average of 1N. This is attributed to the difference in size between the two objects. The transition from being gripped to being pushed away for the spheroid happens a lot more gradually than it did for the ball which is likely due to the spheroid being much smaller, allowing for the fingers to wrap around it rather than only partially grip it like the ball.

Figure 4.23 shows one load versus extension test performed for the straight rod. The average max grip force for this object was nearly 0.52N, the sharp drops indicating where a finger fully loses its grip on the object. This grip adjusting behavior is seen much more clearly in the results of the second grip test compared to the first. The results of the bent rod shown in Figure 4.25, show that Starfish is much more capable of maintaining a stronger grip for a longer duration than the straight rod, with an average maximum grip force of 1N. Since the only difference between the straight rod and the bent rod is the use of a 45° connector piece instead of the straight one, this half a newton increase in strength is likely a result of being grabbed around the angle of the

bent rod. This angle allows Starfish to form a better grip around the rod. One additional thing that could be causing this difference in results is the clamp of the Ametek machine, shown in Figure 5.1 below. Due to how the two different rods are positioned in the clamp, the angle of the bent rod allows the fingers more space to wrap around it while the straight rod does not allow for this. In the image of the straight rod, it can be seen that the fingers are stopped by the clamp.

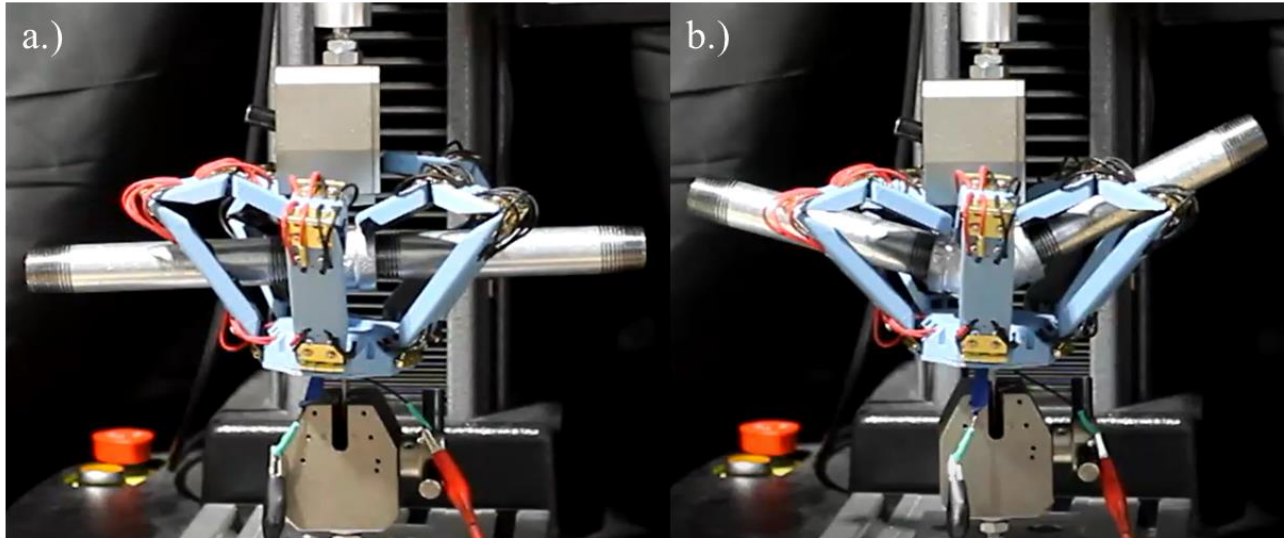


Figure 0.1 Capture of the straight rod a) versus the capture of the bent rod b). The prevention of the fingers from fully closing around the straight rod by the clamp can be seen.

Figure 4.28 shows the average load versus extension results of all ten tests for the bent plate. While the other four plots may have one or two outliers in the data, this plot has the largest variance between all ten of its tests. While the overall shape of each test is roughly the same, the magnitude of the grip force is not. This is likely because of how Starfish was gripping the bent plate. As shown in Figure 5.2, three of the fingers are consistently able to get a solid hold on one side of the plate while the two on the left are not since they are pushed all the way down during capture.

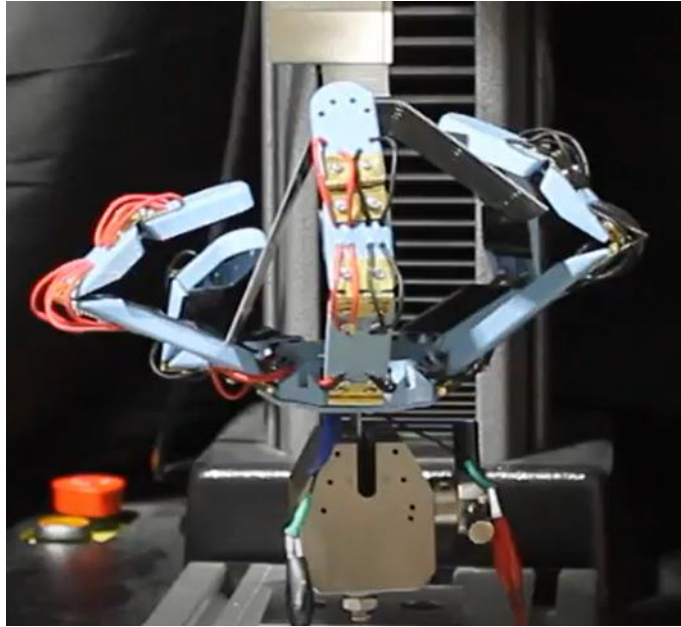


Figure 0.2 Image of Starfish at the end of capturing the bent plate. The two left fingers do not have a solid grasp on the object due to the plate pushing them flat while the center and right most fingers have a better grasp.

As the bent plate is pulled from Starfish's grip the two left most fingers begin to close around the plate since they are no longer being pushed down, increasing the grip strength. However, if the center or right most fingers lose their grip on the object before this occurs, the overall grip strength decreases. The higher grip forces in the tests shown in Figure 4.28 are the result of scenarios where all fingers maintain their grip after the left most fingers close around the object while the lower forces are a result of one or more fingers dropping off before the left most fingers can gain a hold of the object. One other thing to note is that during some of the tests, the corners of the bent plate would become stuck in between the joints of some of the fingers, causing them to maintain a hold and extend further than if this had not occurred. No intervention was required to dislodge the fingers from the bent plate during these tests as the plate would still break loose before it seemed any damage would occur to Starfish.

The final plot shown in Figure 4.29 shows the results of one test performed on the flat plate. From all ten tests for the flat plate two tests reached exceptionally high loads as they were

the result of the flat plate becoming lodged in between multiple finger joints. This caused the fingers to overextend since the plate was not able to free itself and the fingers had to be manually removed to prevent any damage from occurring to Starfish. An image of this occurring during these tests can be seen in Figure 5.3 below.

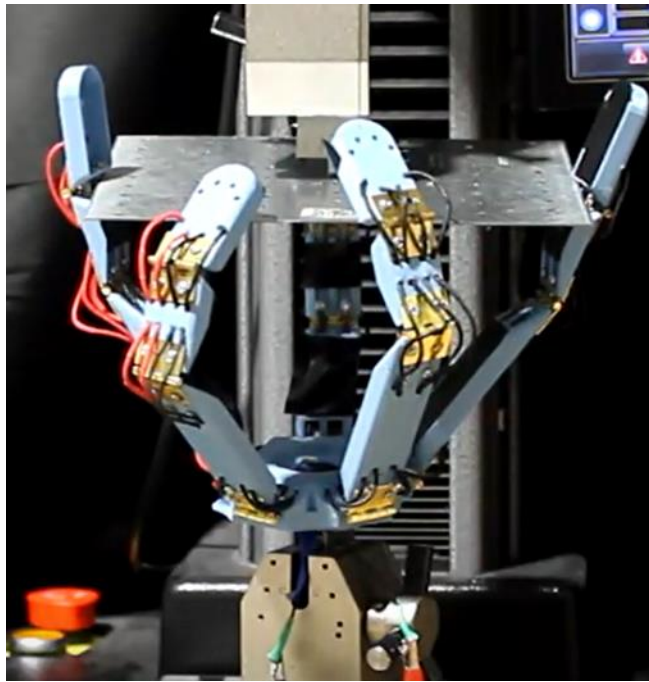


Figure 0.3 Image of the flat plate becoming lodged between multiple joints and beginning to overextend the fingers.

While this does demonstrate that in a mission scenario Starfish is an effective capture technique for this category of debris, it is not beneficial for this type of testing as it could result in the damage of Starfish or the testing apparatus. Regardless of this issue, the flat plate still had the highest grip force of all ten objects tested due to Starfish being able to achieve the most effective initial grip on the object.

5.2 Conclusions

After analyzing the results of all five of these actual debris-based objects it can be seen that Starfish excels at capturing objects with distinct edges such as the flat plates and bent plates. This is consistent with the results of the first grip test wherein Starfish also excelled at gripping

the cube. When compared to the population percentage values from Table 3.3 this shows that Starfish can effectively capture and maintain a sturdy grip on 39% of the orbital debris population. Starfish was shown to be somewhat effective in capturing and maintaining a grip on cylindrical objects such as bent and straight rods, demonstrating that it could be somewhat capable at capturing 42% of the orbital debris population. As previously mentioned, the capture of cylindrical objects was greatly hindered by the use of short grip tabs as it prevented all of the fingers from closing around these objects. If the cylindrical objects were tested again using longer grip tabs, then it is expected that increased capture ability and grip strength would occur. Due to Starfishes low power requirements, it has demonstrated the capability to initiate its capture cycle 50 times with minimal decrease in performance. Therefore, it is more than possible that for these 42% of objects that Starfish could initiate capture multiple times until an effective enough capture occurs. Finally, it was demonstrated that Starfish is least capable of capturing spherical/ “Nugget” shaped items which represent about 19% of the orbital debris population. Overall, this means that Starfish can be used to capture 81% of the orbital debris shapes population.

5.2.1 Comparison of Starfish to Current ADR Methods

As most ADR concepts are theoretical, there is not much out there about grip strength or capture time for each method. Therefore, these comparisons will be based off of what is known. Firstly, when compared to magnet-based ADR methods, this method is also not limited to shape or size. However, it is limited to only debris comprised of magnetic materials. Table 5.1 shows a material breakdown for the known material compositions of orbital debris objects.

Table 5.1 Material composition of orbital debris objects [20].

SOCIT4 Material	%	DebrisSat Material	%	Category	Density
		○ CFRP	61%	CFRP	1.5 g/cm ³
<ul style="list-style-type: none"> ● Fiberglass ● Phenolic/Plastic 	8% 68%	○ Epoxy	6%	Low Density (LD)	< 2 g/cm ³
		○ Polyimide film	0.8%		
		○ Para-aramid synthetic fiber	0.4%		
		○ Multi-Layer Insulation, MLI	4%		
		○ Printed Circuit Board, PCB	1%		
		○ Plastic	6%		
		○ Silicon	0.8%		
<ul style="list-style-type: none"> ● Al ● Other 	22% 1%	○ Al	5%	Medium-Low Density (MD-lo)	2–4 g/cm ³
		○ Glass	1%		
		○ <i>Metal</i>	2%		
		○ Solar Cell	0.4%		
		○ Titanium	1%	Medium-High Density (MD-hi)	4–6 g/cm ³
<ul style="list-style-type: none"> ● Copper ● Steel 	0.3% 0.7%	○ Copper	9%	High Density (HD)	> 6 g/cm ³
		○ Steel)	2%		
	100%		100%		

*DebrisSat database contents as of January 27, 2023.

From this table it can be seen that a majority of the materials that comprise the orbital debris environment are not magnetic. Therefore, Starfish is capable of capturing 96% while magnetic ADR methods are only capable of capturing 4% of the orbital debris population. Starfish has been demonstrated to be able to perform its capture cycle 50 times without notable failure. This is a significant advantage over other ADR methods such as the net or harpoon that can only perform their capture cycle one to two times per mission. Starfish only requires 36-40 watts of power for two minutes to perform a capture. When compared to other ADR methods that require significant power to operate such as space lasers and soft attachment methods, this is a significant advantage.

5.3 Recommendations

The most prevalent issue in these experiments was the heat emitted from the wires. While the mechanical ability of Starfish was proven, it was hindered every step of the way by the threat components melting together or full material breakdown. Though a full-scale metal modal of Starfish would mitigate some of the issues that result from the heat generation, it would not wholly prevent it. Therefore, it is recommended that any future iterations of this design include

the addition of a cooling system for the wires. The internal structure of the base plate and fingers are already nearly hollow and could be utilized for housing such a cooling system. As Starfish is meant for long-term space applications, research should begin with investigating appropriate cooling systems already being used in the current space environment. It would also be beneficial to research how SMA's are kept cool in soft robotic applications as well.

Another useful addition that could be made is to add magnetic pads to the palm side of Starfishes fingers in order to maintain a better grip on debris that is comprised of magnetic materials. An external skin/membrane covering is needed to protect Starfishes components from the space environment and could also serve as a container for a cooling system. Thicker PETG finger shells would not melt as easily as the thin shelled ones.

Future tests of Starfish should focus on conducting tests with three different sized objects of the same category and in different orientations in order to determine the best method of capture for each object category. Additionally, Starfish's ability to capture tumbling objects should be tested.

6 REFERENCES

- [1] Kessler, D. J., and Cour-Palais, B. G., “Collision frequency of artificial satellites: The creation of a debris belt,” *Journal of Geophysical Research: Space Physics*, vol. 83, 1978, pp. 2637–2646.
- [2] Maclay, T., and McKnight, D., “Space Environment Management: Framing the objective and setting priorities for controlling orbital debris risk,” *Journal of Space Safety Engineering*, vol. 8, Mar. 2021, pp. 93–97.
- [3] Robert, Bosch, and Strasse, “ESA’s space environment report 2023,” ESA Available: https://www.esa.int/Space_Safety/ESA_s_Space_Environment_Report_2023.
- [4] Adushkin, V. V., Aksenov, O. Yu., Veniaminov, S. S., Kozlov, S. I., and Tyurenkova, V. V., “The small orbital debris population and its impact on space activities and ecological safety,” *Acta Astronautica*, vol. 176, 2020, pp. 591–597.
- [5] “Hubble’s impactful life alongside Space Debris,” ESA Available: https://www.esa.int/Space_Safety/Hubble_s_impactful_life_alongside_space_debris
- [6] Orbital Debris Program, Anz-Meador, P., Jacobs, J., and Liou, J.-C., Houston, Texas: National Aeronautics and Space Administration, 2022.
- [7] Bongers, A., and Torres, J. L., “Star wars: Anti-satellite weapons and orbital debris,” *Defence and Peace Economics*, Apr. 2023, pp. 1–20.
- [8] Valencia, S., "Analyses of the Russian antisatellite ASAT missile test on Kosmos-1408 and its impact on space sustainability", 2021.
- [9] Elliot, J. K., “Canadarm2 damaged by ‘lucky strike’ from space junk in orbit,” *Global News*, Jun. 2021
- [10] Krag, H., Serrano, M., Braun, V., Kuchynka, P., Catania, M., Siminski, J., Schimmerohn, M., Marc, X., Kuijper, D., Shurmer, I., O’Connell, A., Otten, M., Muñoz, I., Morales, J., Wermuth, M., and McKissock, D., “A 1 cm space debris impact onto the sentinel-1a solar array,” *Acta Astronautica*, vol. 137, 2017, pp. 434–443.
- [11] Joubert, W., and Tingay, S., “Simulations of orbital debris clouds due to breakup events and their characterisation using the Murchison Widefield Array Radio Telescope,” *Experimental Astronomy*, vol. 51, Nov. 2020, pp. 61–75.
- [12] Anz-Meador, P., Opiela, J., and Liou, J.-C., Houston, Texas: NASA Johnson Space Center, 2022.
- [13] Oltrogge, D., Alfano, S., and Hall, R., "Comparison of predicted and observed spacecraft encounters from Russian ASAT test", COMSPOC Corporation, 2022.

- [14] “ESA’s space environment report 2021,” ESA Available: https://www.esa.int/Space_Safety/Space_Debris/ESA_s_Space_Environment_Report_2021.
- [15] Aglietti, G. S., Taylor, B., Fellowes, S., Salmon, T., Retat, I., Hall, A., Chabot, T., Pisseloup, A., Cox, C., Zarkesh, A., Mafficini, A., Vinkoff, N., Bashford, K., Bernal, C., Chaumette, F., Pollini, A., and Steyn, W. H., “The active space debris removal mission removedebris. part 2: In Orbit Operations,” *Acta Astronautica*, vol. 168, 2020, pp. 310–322.
- [16] Scott, “Astroscale, securing Space Sustainability,” Astroscale Available: <https://astroscale.com/>.
- [17] Bonnal, C., Ruault, J.-M., and Desjean, M.-C., “Active debris removal: Recent progress and current trends,” *Acta Astronautica*, vol. 85, 2013, pp. 51–60
- [18] Jurado, R., Pallarès, J., Gavaldà, J., and Ruiz, X., “On the impact of the ISS reboosting maneuvers during thermodiffusion experiments of ternary liquid systems: Pure diffusion,” *International Journal of Thermal Sciences*, vol. 132, Oct. 2018, pp. 186–198.
- [19] Radtke, J., Domínguez-González, R., Flegel, S. K., Sánchez-Ortiz, N., and Merz, K., “Impact of eccentricity build-up and graveyard disposal strategies on MEO Navigation Constellations,” *Advances in Space Research*, vol. 56, Dec. 2015, pp. 2626–2644.
- [20] Seago, J., Cowardin, H., Anz-Meador, P., Manis, A., Miller, J., and Christansen, E., “2nd Orbital Debris Conference,” 2023.
- [21] Poozhiyil, M., Nair, M. H., Rai, M. C., Hall, A., Meringolo, C., Shilton, M., Kay, S., Forte, D., Sweeting, M., Antoniou, N., and Irwin, V., “Active debris removal: A review and case study on Leopard Phase 0-A mission,” *Advances in Space Research*, vol. 72, Oct. 2023, pp. 3386–3413.
- [22] Zhang, W., Li, F., Li, J., and Cheng, Q., “Review of on-orbit robotic arm active debris capture removal methods,” *Aerospace*, vol. 10, Dec. 2022, p. 13.
- [23] Shan, M., Guo, J., and Gill, E., “Review and comparison of active space debris capturing and removal methods,” *Progress in Aerospace Sciences*, vol. 80, Jan. 2016, pp. 18–32.
- [24] Biesbroek, R., Aziz, S., Wolahan, A., Cipolla, S., Richard-Noca, M., and Piguet, L., “8th European Conference on Space Debris,” ESA Space Debris Office, 2021.
- [25] Trushlyakov, V., and Yudintsev, V., “Dynamics of rotating tethered system for active debris removal,” *Acta Astronautica*, vol. 195, Jun. 2022, pp. 405–415.
- [26] Valmorbida, A., Olivieri, L., Brunello, A., Sarego, G., Sánchez-Arriaga, G., and Lorenzini, E. C., “Validation of enabling technologies for deorbiting devices based on electrodynamic tethers,” *Acta Astronautica*, vol. 198, Sep. 2022, pp. 707–719.

- [27] Sarego, G., Olivieri, L., Valmorbida, A., Brunello, A., Lorenzini, E. C., Tarabini Castellani, L., Urgoiti, E., Ortega, A., Borderes-Motta, G., and Sánchez-Arriaga, G., “Deployment requirements for deorbiting electrodynamic tether technology,” *CEAS Space Journal*, vol. 13, Feb. 2021, pp. 567–581.
- [28] Ledkov, A., and Aslanov, V., “Review of Contact and contactless active space debris removal approaches,” *Progress in Aerospace Sciences*, vol. 134, Oct. 2022, p. 100858.
- [29] Shan, M., Guo, J., and Gill, E., “Deployment Dynamics of tethered-net for space debris removal,” *Acta Astronautica*, vol. 132, Mar. 2017, pp. 293–302.
- [30] Schaub, H., and Sternovsky, Z., “Active space debris charging for contactless electrostatic disposal maneuvers,” *Advances in Space Research*, vol. 53, Jan. 2014, pp. 110–118.
- [31] Andrenucci, M., Pergola, P., Ruggiero, A., Olympio, J., & Summerer, L., “Active Removal of Space Debris: Expanding foam application for active debris removal,” *ESA Final Report*, 132, 2011.
- [32] Busche, J. F., Starke, G., Knickmeier, S., and Dietzel, A., “Controllable dry adhesion based on two-photon polymerization and replication molding for space debris removal,” *Micro and Nano Engineering*, vol. 7, Jun. 2020, p. 100052.
- [33] Mark, C. P., and Kamath, S., “Review of active space debris removal methods,” *Space Policy*, vol. 47, Feb. 2019, pp. 194–206.
- [34] Svitina, V. V., and Cherkasova, M. V., “Space debris removal – review of technologies and techniques. flexible or virtual connection between space debris and service spacecraft,” *Acta Astronautica*, vol. 204, Mar. 2023, pp. 840–853.
- [35] Dudziak, R., Tuttle, S., and Barraclough, S., “Harpoon technology development for the active removal of space debris,” *Advances in Space Research*, vol. 56, Aug. 2015, pp. 509–527.
- [36] Lathia, M. D., and Dakka, S. M., “Space harpoon projectile analysis for space debris capture,” *The International Journal of Aviation, Aeronautics, and Aerospace*, 2014.
- [37] Serfontein, Z., Kingston, J., Hobbs, S., Holbrough, I. E., and Beck, J. C., “Drag augmentation systems for space debris mitigation,” *Acta Astronautica*, vol. 188, Nov. 2021, pp. 278–288.
- [38] “ClearSpace-1 VESPA Apparently Hit By Orbital Space Debris,” *SpaceRef.com*, Aug. 2023.
- [39] M Balasubramanian et al 2021 *J. Phys.: Conf. Ser.* 2054 012078
- [40] Costanza, G., and Tata, M. E., “Shape memory alloys for aerospace, recent developments, and new applications: A short review,” *Materials*, vol. 13, Apr. 2020, p. 1856.

- [41] Concilio, A., Antonucci, V., Auricchio, F., Lecce, L., and Sacco, E., “Phenomenology of Shape Memory Alloys,” *Shape Memory Alloy Engineering: For Aerospace, Structural, and Biomedical*, Cambridge, MA: Elsevier, 2021, pp. 115–127.
- [42] Kim, D., “Shape Memory Alloys,” *Powerpoint slides for SMART Materials class, fall 2022, Embry-Riddle Aeronautical University*
- [43] Garcia, E., “smart structures and actuators: Past, present, and future,” *Smart Structures and Materials 2002: Industrial and Commercial Applications of Smart Structures Technologies*, Jul. 2002.
- [44] Hartl, D. J., and Lagoudas, D. C., “Characterization and 3-D modeling of NI60TI SMA for actuation of a variable geometry jet engine chevron,” *SPIE Proceedings*, Apr. 2007.
- [45] Chavan, S., and Gujar, P., “Shape memory alloy actuators are used to create a variable area jet nozzle for noise reduction: A Review,” *International Journal of Engineering Applied Sciences and Technology*, vol. 6, Jul. 2021.
- [46] Kwon, S.-C., Jeon, S.-H., and Oh, H.-U., “Performance evaluation of spaceborne cryocooler micro-vibration isolation system employing pseudoelastic SMA mesh washer,” *Cryogenics*, vol. 67, Apr. 2015, pp. 19–27.
- [47] Carpenter, B., & Lyons, J., “EO-1 technology validation report: Lightweight flexible solar array experiment”. *NASA/GSFC*, 2001.
- [48] Naghipour, P., Santo Padula, I. I., Creager, C., & Oravec, H., “Development and Implementation of Large-Scale Numerical Models for Shape Memory Mars Spring Tires”, No. E-20139, 2024.
- [49] Martin, T., Omar, S., and Bevilacqua, R., “Controlled spacecraft re-entry of a Drag De-Orbit Device (D3),” *UF Journal of Undergraduate Research*, vol. 21, Dec. 2019.
- [50] “Hand anatomy,” Video | Medical Video Library [online database], URL: https://www.ypo.education/orthopaedics/hand_wrist/hand-anatomy-t191/video/ [retrieved 10 May 2023]
- [51] Dynalloy Inc., “Technical Characteristics of Flexional Actuator Wires.”
- [52] Zak, A. J., Cartmell, M. P., Ostachowicz, W. M., and Wiercigroch, M., “One-dimensional shape memory alloy models for use with reinforced composite structures,” *Smart Materials and Structures*, vol. 12, Apr. 2003, pp. 338–346.
- [53] Bundhoo, V., Haslam, E., Birch, B., and Park, E. J., “A shape memory alloy-based tendon-driven actuation system for biomimetic artificial fingers, part I: Design and evaluation,” *Robotica*, vol. 27, Jan. 2009, pp. 131–146.

- [54] Simone, F., Rizzello, G., Seelecke, S., and Motzki, P., “A soft five-fingered hand actuated by shape memory alloy wires: Design, manufacturing, and Evaluation,” *Frontiers in Robotics and AI*, vol. 7, Dec. 2020.

7 PUBLICATIONS

Branaman, K., and Kim, D., “Starfish: A compact, biomimetic, and shape memory actuated orbital debris remover,” *AIAA SCITECH 2024 Forum*, Jan. 2024.

Branaman, K., and Kim, D., “Starfish: An Orbital Debris Remover,” *ICSSA 2024 Conference*, May 2024.